

Review

On the Morphology of Nanostructured TiO₂ for Energy Applications: The Shape of the Ubiquitous Nanomaterial

Serena Gagliardi , Flaminia Rondino , Claudia Paoletti  and Mauro Falconieri * 

ENEA, The Italian National Agency for New Technologies, Energy and Sustainable Economic Development, C.R. Casaccia, Via Anguillarese 301, 00123 Rome, Italy; serena.gagliardi@enea.it (S.G.); flaminia.rondino@enea.it (F.R.); claudia.paoletti@enea.it (C.P.)

* Correspondence: mauro.falconieri@enea.it; Tel.: +39-06-30486285

Abstract: Nanostructured titania is one of the most commonly encountered constituents of nanotechnology devices for use in energy-related applications, due to its intrinsic functional properties as a semiconductor and to other favorable characteristics such as ease of production, low toxicity and chemical stability, among others. Notwithstanding this diffusion, the quest for improved understanding of the physical and chemical mechanisms governing the material properties and thus its performance in devices is still active, as testified by the large number of dedicated papers that continue to be published. In this framework, we consider and analyze here the effects of the material morphology and structure in determining the energy transport phenomena as cross-cutting properties in some of the most important nanophase titania applications in the energy field, namely photovoltaic conversion, hydrogen generation by photoelectrochemical water splitting and thermal management by nanofluids. For these applications, charge transport, light transport (or propagation) and thermal transport are limiting factors for the attainable performances, whose dependence on the material structural properties is reviewed here on its own. This work aims to fill the gap existing among the many studies dealing with the separate applications in the hope of stimulating novel cross-fertilization approaches in this research field.

Keywords: nanophase TiO₂; dye-sensitized solar cells; perovskite solar cells; nanofluids; photoelectrochemical water splitting



Citation: Gagliardi, S.; Rondino, F.; Paoletti, C.; Falconieri, M. On the Morphology of Nanostructured TiO₂ for Energy Applications: The Shape of the Ubiquitous Nanomaterial.

Nanomaterials **2022**, *12*, 2608.

<https://doi.org/10.3390/nano12152608>

nano12152608

Academic Editor: Andreu Cabot

Received: 30 June 2022

Accepted: 22 July 2022

Published: 29 July 2022

Publisher's Note: MDPI stays neutral with regard to jurisdictional claims in published maps and institutional affiliations.



Copyright: © 2022 by the authors. Licensee MDPI, Basel, Switzerland. This article is an open access article distributed under the terms and conditions of the Creative Commons Attribution (CC BY) license (<https://creativecommons.org/licenses/by/4.0/>).

1. Introduction

In the ever-growing world of chemical compounds entering the nanomaterials domain, titanium dioxide is undoubtedly one of the oldest and most widely used. Starting from its former use as white pigment in paints and inks, this material has found its way into applications ranging from energy conversion to environmental and chemical engineering, sensors, consumer products and medical care [1–3]. As such, nanostructured TiO₂ is presently one of the most ubiquitous and multifunctional components in the nanotechnology world. Correspondingly, a huge number of related research papers have been published in the literature, and many topical reviews have appeared to assess the current state-of-the-art and also give a historical perspective of the advancements; for instance, recent review papers have been published concerning nanophase TiO₂ applications in photovoltaics [4] and photocatalysis [5], rechargeable batteries [6], sensors [7] and biosensors [8,9] and biomedicine [10]. Despite this ubiquity, the possibilities to tailor the material properties rely mainly on its nanophase-specific features, considering its fixed and stable chemistry and apart from the possibility of stoichiometric or compositional doping, whose functionality is still largely a matter of investigation [11]. As for its bulk properties, TiO₂ has three crystalline polymorphs at ambient pressure, i.e., brookite, anatase and rutile [12], whose suitability for various applications is still somewhat of a matter of investigation (pp. 1–240, [13]), [14,15]; notwithstanding this situation, anatase is the most used in practice for many applications

due to its ease of fabrication as nanophase and its intrinsic electronic energy properties [15]. In contrast, when it comes to the nanophase-specific features, the surface properties and the material morphology and structure add a great number of degrees of freedom and are of the utmost importance to implement specific functionalities for different applications. For example, surface termination controls the hydrophilic–hydrophobic behavior that is important for self-cleaning, photocatalytic and biological applications; moreover, it can be used to create surface trap states that are useful to control the spatial distribution of electrons and holes, which is of paramount importance in electrochemical and electronic applications. On the other hand, the morphology, i.e., the form of the basic nanophase unit forming the material, be it a bead, nanotube, needle etc., and its nanostructure, i.e., how the basic units are arranged, such as fractal aggregates, hierarchical arrangements, ordered structures etc., ultimately determines fundamental functional properties such as the optical behavior and the electronic and thermal transport. Therefore, for many applications, the material morphology and structure are the driving factors for optimized performances; this evidence constitutes the scientific basis of the present work.

According to this point of view, here we present a review on the role played by the morphology and structure of TiO₂ in selected applications in the field of energy where the transport and optical phenomena are of the utmost importance, namely photovoltaic energy conversion by dye-sensitized and perovskite solar cells, photoelectrochemical water splitting and nanofluids for thermal management. While recent reviews [4–10] focused on separate and specific applications of TiO₂, this review aims to account for the state of the art of the research describing the structural effects in such apparently different fields with a novel approach. As a matter of fact, reviews on the impact of the structural aspects of nanophase TiO₂ on some of its applications have appeared in the literature and have mainly focused on mesoporous structures [16], thus excluding dispersions and without paying specific attention to the related transport phenomena. These aspects are instead extensively covered in the present work.

Currently, a comprehensive picture of the relationship between the material morphology/structure and its optical, electronic and thermal transport properties is yet to be achieved due to the interplay among properties and to the variety of configurations with the consequent difficulty of obtaining a realistic material description. Nevertheless, we believe that the present updated review of the experimental and, where available, theoretical works, delineating significant trends in such vast and disperse topics, can boost the exploitation of titania-nanostructures in the field of energy applications.

2. Photovoltaic Energy Conversion

Among the many different photovoltaic technologies, we focus here our attention only on those where nanostructured TiO₂ is a core component, namely dye-sensitized solar cells (DSSCs) and perovskite solar cells (PSCs).

Photovoltaic energy conversion by dye-sensitized semiconductors has been widely investigated [17,18] since the last decades of the past century, but, until the publication of the paper by O'Regan and Gratzel in 1991, which reported a conversion efficiency of 7% [19], these systems typically achieved efficiency values that were too small for practical use. The disruptive idea was the replacement of a flat surface bulk semiconductor with a nanostructured photoanode (PA) with a very high surface area, allowing high dye load and consequently high light absorption. The PA in the DSSCs is a mesoporous film made of nanosized TiO₂ beads sintered on a transparent conductive oxide (TCO) placed on a glass substrate and has a double functionality: it is both the supporting medium of the molecular light absorber (i.e., the dye) and the electron acceptor and transport layer; see Figure 1.

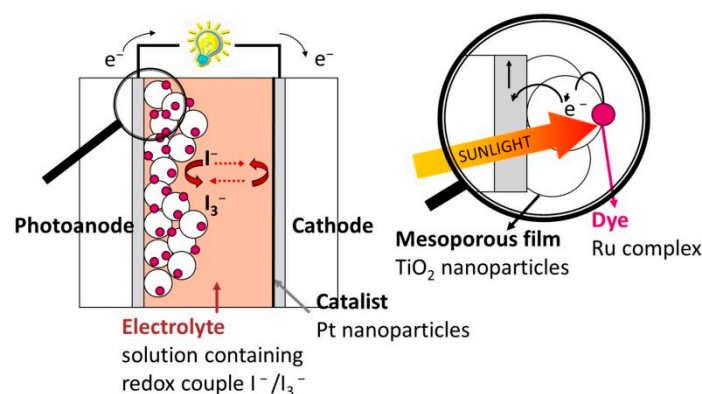


Figure 1. Schematics of a DSSC (left) and detail of the photoanode (right). A comprehensive review of the operating principles of a DSSC is reported in [20].

The first functionality requires a high specific surface area, attainable in principle by decreasing the titania nanoparticle size, and mainly determines the maximum short circuit current density J_{sc} in the ideal condition whereby all the photogenerated carriers are collected at the electrodes, given by [20]:

$$J_{sc} = q \int_{\lambda_{min}}^{\lambda_{MAX}} F(\lambda) [(1 - R(\lambda))] A(\lambda) d\lambda \quad (1)$$

where q is the electron charge, $F(\lambda)$ is the incident light spectral distribution, and $R(\lambda)$, $A(\lambda)$ are the device spectral reflectivity and the sensitized PA light absorption, respectively. The most used dyes, typically Ru-based organometallic molecules, allow light harvesting in the visible region and have a molar absorption coefficient of $10^7 \text{ cm}^{-1} \text{ mol}^{-1}$ [19,21], meaning that the mesoporous titania layer thickness needed to achieve reasonable light-harvesting, for practically achievable surface areas, is about $10 \mu\text{m}$. Even employing new organic sensitizers with higher absorption coefficients, the thinnest TiO_2 PA is on the order of $5 \mu\text{m}$ [22,23]. Furthermore, since a large part of solar radiation is lost due to the poor dye absorption at long wavelengths, many research efforts have been devoted both to the synthesis of novel dyes with extended absorption in the infrared and co-sensitization to attain panchromatic absorption [23–25] to improve photocurrent and hence overall conversion efficiency. However, at the same time, techniques enhancing light diffusion phenomena within the PA have been implemented to improve the light absorption by increasing the photon path, exploiting the so-called light trapping (LT) effect. Since light scattering is strongly dependent on the dimension and shape of the scatterer, it can be argued that it can be optimized by tailoring the morphology and structure of the titania film, e.g., changing nanoparticles' dimensions, arrangement and aspect ratio, maximizing accordingly the optical absorption in the PA and hence improving the cell performance, as widely discussed in Section 2.1.

The morphology, noticeably, also strongly influences the second functionality of PA, i.e., the electron transport toward the TCO collecting electrode [20,26]. As a matter of fact, the electron transport along the PA thickness is strongly affected by the nanostructure: the tortuous path and the electron traps related to surface states indeed limit the electrons' mobility and constitute a bottleneck in the amelioration of the conversion efficiency of DSSCs.

Hence, huge efforts, which are detailed in the following, were devoted to the study of how the structure and the morphology of the TiO_2 PA (i.e., dimensions and organization of nanobeads, use of hierarchical organization, use of 2D nanostructures as nanotubes and nanowires) impact on its functional properties, in order to realize high efficiency dye-sensitized solar cells.

A couple of decades after the publication of the O'Reagan and Graetzel paper [19], in 2012, the introduction by Snaith and coworkers [27] of an organometal halide perovskite

extremely thin absorber infiltrated in the mesoporous titania electrode newly set up the photovoltaic research field. The perovskite absorption coefficient is one order of magnitude higher than that of organometallic dyes, so the thickness necessary for efficient light-harvesting is only some hundreds of nanometers. This down-scaling of the mesoporous titania layer thickness changed the functional requirements, as discussed in the following, meaning that the optimization strategies to achieve high conversion efficiency have been changed accordingly.

In this section, after a brief account of the theoretical background, we review selected examples of the effects of the morphology of the nanostructured titania on both the optical and transport properties of the PA in a DSSC and therefore ultimately on the device conversion efficiency; then, we discuss how some of these concepts were overcome in thinner electrodes in PSC, showing how all the knowledge achieved in more than two decades of research on nanostructured titania electrodes for DSSCs has been transferred into the development of PSCs.

2.1. Light Management

The increased absorption resulting from the tendency of light to be trapped by multiple internal reflections in textured surfaces semiconductors was initially exploited in silicon photodetectors and solar cells [28]. In 1981, Yablonovitch [29] proposed the first analytical approach to quantify the effect of light trapping on the interaction of radiation with scattering materials, focusing on the optical properties of media with tailored surface shapes or random surface structures. The enhancement of LT in thin film solar cells is typically achieved by a textured metal back-reflector that scatters light within the absorber layer and increases the optical path length of solar photons [30]. In DSSCs, the most commonly used dye, N719, i.e., di-tetrabutylammonium cis-bis(isothiocyanato)bis(2,2'-bipyridyl-4,4'-dicarboxylato)ruthenium(II), has a low absorption coefficient for red or longer wavelengths [21], meaning that the use of LT has become a standard practice to increase the optical path length in the cell at long wavelengths.

The beneficial presence of light diffusion effects in DSSCs was first theoretically analyzed by Usami [31,32] and Ferber [33]. A simple schematic of the LT process is reported in Figure 2. The exact general solution of light scattering by a particle was obtained by Mie but, since it applies to an isotropic and homogeneous sphere, it is not adequate for the TiO₂ porous film. Usami examined the scattering of a single titania particle and then derived contributions from multiple particles using the Monte Carlo simulation method. The results indicated that optimal conditions for backscattering were consistent with the total reflection at the interface between the TiO₂ thin film and the glass substrate. This led to the conclusion that useful optical confinement in the active layer can be achieved by inserting a reflecting TiO₂ (rutile phase) thin film between the TCO and glass substrate and covering the PA with a film of large scattering nanoparticles. Rothenberger et al. [34] proposed a thorough optical characterization procedure for porous, thick titania electrodes and an optical model that allows the interpretation of experimental data. Moreover, they calculated a hypothetical maximum photocurrent density, assuming that each absorbed photon yields a collected electron. The optical properties of electrodes composed of a mixture of small (10–25 nm) and large (600–800 nm) particles were analyzed by Ferber. He found that the optimum optical behavior is obtained by adding 5% of larger particles with a radius of 125–150 nm to a small particles-based electrode. Gagliardi and Falconieri [35] proposed an experimental method to calculate a spectral factor to quantify the LT effect, which is useful to disentangle the concurrent light absorption by dye molecules from the scattering phenomena in the mesoporous titania film. Indeed, all the high-efficiency DSSCs based on spherical nanoparticles reported in the literature exploit LT both incorporating an additional scattering film [36–38] to reflect the light not yet absorbed in the active layer and embedding scattering particles in the active layer to increase the light path wavelengths [39–42] by diffusion.

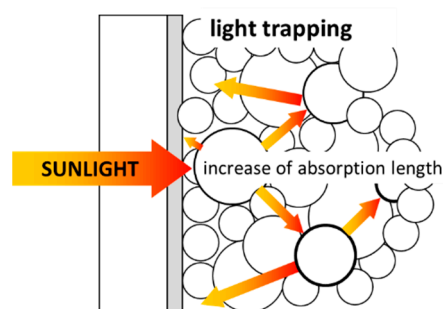


Figure 2. Schematic of the light trapping phenomenon in the nanostructured DSSC photoanode.

Large void spherical structures were also proposed by [43–46] to enhance light scattering within the PA, demonstrating higher light harvesting capabilities compared to small spherical nanobeads-based electrodes. Moreover, a wide variety of TiO₂ different morphologies was used to improve LT phenomena and consequently the conversion efficiency (see Figure 3). High aspect ratio nanostructures such as nanospindles, nanowires, nanofibers and nanotubes have been proposed [47–50]; however, in most of the published literature, any explicit discussion and quantification of the impact of PA morphology on LT is missing, even though improved efficiency values are demonstrated in comparison to “conventional” PA based on small spherical particles. One of the most investigated nanostructures, i.e., titania nanotubes obtained by the electrochemical etching of titanium foils, should deserve its own discussion; here, we recall that the electrochemical process can be tuned to finely tailor the wall dimensions and length of the vertically aligned nanotubes, which grow vertically [51–54] packed in an approximately hexagonal symmetry, as visible in Figure 3. Despite the lower specific surface area with respect to those based on nanoparticles with the same thickness, nanotube PAs were believed to have superior transport properties, allowing the use of thicker films (up to tens of micrometers) to recover the dye load; furthermore, the micrometric dimensions were demonstrated to enhance the internal light scattering, thus improving light harvesting efficiency up to 20% with respect to that obtained with spherical nanoparticle-based films [51–54].

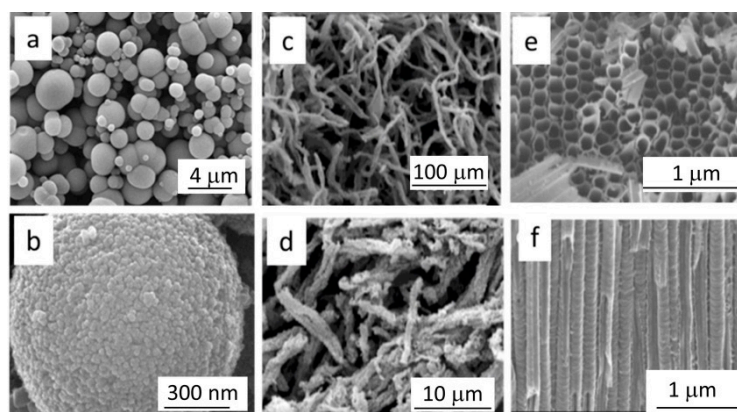


Figure 3. SEM images of examples of DSSCs PAs based on different TiO₂ nanostructures. (a,b) adapted with permission from [43]. Copyright 2008, Wiley & Sons; (c,d) adapted with permission from Ref. [48], Copyright 2010, American Chemical Society; (e,f) adapted with permission from Ref. [53], Copyright 2010, American Chemical Society.

As mentioned before, the introduction of organometallic halide perovskites as light absorbers [27] in 2012 deeply changed the requirement of the titania mesoporous films: perovskites have an absorption coefficient one order of magnitude higher than dyes in the visible spectral region. This implies that a mesoporous titania electrode of a few hundreds of nanometers in thickness, coated with an extremely thin perovskite layer (<10 nm), absorbs

98.4% of 500 nm radiation and produces a high photogenerated current density (i.e., 17.8 mA cm⁻² in 500 nm thick layer [27]). Nevertheless, the perovskite absorption is poor in the infrared spectrum, meaning that proper photon management is still desired in order to increase the generated photocurrent. Even though the morphology of the mesoporous scaffold determines the structure and the functional properties of the perovskite-based PA absorber, the strategies developed for thick film DSSCs, such as proper choice of titania nanoparticles dimensions and/or shape and morphology engineering, are not suitable for the much thinner PA in PSCs. So, novel morphologies of the mesoporous titania scaffolds were poorly investigated for their light diffusive properties, even though 3D flower-shaped [55,56] and hollow sphere [57] nanostructures were demonstrated to improve the light harvesting efficiency by several percent in the low wavelength region. On the other hand, many studies were devoted to the texture of the interface between the TiO₂ layer and the transparent conductive oxide in order to enhance the LT effect and accordingly improve the photocurrent: several papers report on the realization of hemispherical voids or titania structures on well-defined patterns [58–64]. These photonic structures maximize (see Figure 4) the long wavelength light absorption inside the cell and consequently allow higher photocurrent generation, yielding up to 13% improved overall conversion efficiencies.

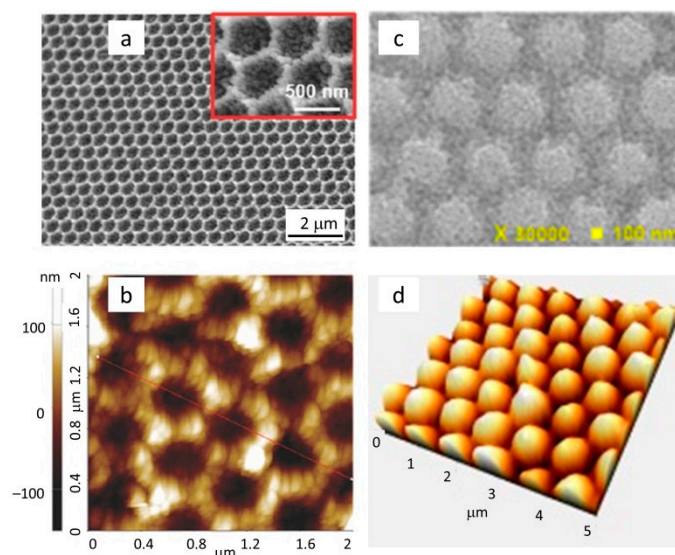


Figure 4. SEM (**top**) and AFM (**bottom**) images of two examples of different titania patterned electrodes in PSCs. (**a,b**) adapted with permission from [59], Copyright 2016, Wiley and Sons; (**c,d**) adapted with permission from Ref. [63], Copyright 2019, Elsevier B. V.

2.2. Transport Properties

In a DSSC, electrons are photoexcited by light absorption in the dye molecules and then injected into the titania nanostructured film, where they travel until they are collected by the TCO. The nanostructured PA has a high internal surface area in contact with the electrolyte, which screens the electric field [65], meaning that the travel of the electron from a nanoparticle to another is a random walk between equivalent sites and may be considered a diffusive process [66–68]. This picture is consistent with the experimental values measured for the electron diffusion coefficient D , which is found to be one or two orders of magnitude lower than that expected for a bulk single crystal of TiO₂ [69,70]. For this reason, understanding the dependence of the electron transport efficiency in the porous film on the network topology [71,72] and on the grain morphology [69] is of uppermost importance for the improvement of solar cells conversion efficiency. To this end, several papers discuss the electron transport using models based on a random walk approach, in

which the electron diffusion coefficient D is related to the film porosity P according to the percolation theory [71]:

$$D = a|P - P_C|^\mu \quad (2)$$

where a is a constant containing information about the average distance between connected particles and the electron residence time in a particle, P_C is the critical porosity above which the film is not continuous, and μ is the power-law exponent associated with the conduction mechanism. As the film porosity increases, the coordination number decreases, leading to a tortuous and longer electron pathway, increasing the number of particles visited by electrons and increasing the fraction of dead-end particles. Transient photocurrent measurements confirm the model predictions, obtaining values of D that decrease from $\approx 5 \cdot 10^{-3} \text{ cm}^2 \text{ s}^{-1}$ to $\approx 5 \cdot 10^{-4} \text{ cm}^2 \text{ s}^{-1}$ at 1 sun illumination when the porosity increases from 0.5, i.e., the typical value in DSSC PAs, to 0.8, close to the critical porosity value. On the other hand, the value obtained for the power-law coefficient by fitting the experimental data with the percolation model is much lower than that expected for random mixtures, suggesting that a rearrangement of the nanoparticles occurs during the sintering process, preventing the formation of isolated clusters.

On the other hand, the experimental observation of slow transport, with time constants ranging from milliseconds to seconds and a small diffusion coefficient, both depending on the illumination intensity [73,74], shows the existence of a trap-limited transport mechanism [66,75–85]. This transport mechanism, due to electron trapping and detrapping processes in an exponential density of band gap states, was actually demonstrated with different experimental techniques, such as transient photocurrent measurements [66,73,78,86], intensity modulated photocurrent spectroscopy [73,74,77,78,81,87] and current–voltage measurements [67,77,82].

With the aim of improving the overall conversion efficiency of DSSC by optimizing the conductive properties of the PA, the spherical nanoparticles were frequently substituted with randomly organized elongated nanostructures, such as nanowires [88,89], hollow fibers [48] and nanospindles [49] or also well-ordered vertically oriented nanotubes [90,91]. For electrochemically synthesized and vertically oriented nanotubes, the morphology implies a significant reduction in the specific surface area and hence the necessity of much thicker PAs to achieve comparable dye load. Amorphous titania nanotubes are grown by titanium anodization, and the crystallization is achieved by subsequent thermal annealing in oxygen. Growing titania nanostructures from a Ti foil gives a non-transparent anode which is to be implemented in the so-called back-illuminated DSSCs, where the light losses due to undesired light absorption in the counter electrode and in the electrolyte decrease the generated photocurrent; to avoid this geometry, Ti films were first deposited on the transparent conductive oxide, then anodized and finally annealed. In this way, nanotube-based PAs were realized and implemented in DSSCs. Nevertheless, the efficiency of these solar cells was not much better than those realized with conventional electrodes, even though PA thickness was reported to reach 33 μm , thus compensating for the otherwise small dye load [90,91]. The unexpectedly poor performance as the DSSC anode of the ordered nanotubes arrays was attributed to the deterioration of the TCO occurring during the thermal treatment of the titania nanotubes but also to the high density and deepness of the traps that degrade the transport properties of the film, pointing out the need for a technical improvement in the realization steps.

Titania nanotubes were also mixed with nanoparticles after detachment from the titanium foil, and the PA made of this mixture was demonstrated to perform slightly better than a conventional PA only for a relatively small number of nanotubes (10 wt%) [92]; indeed, for high concentrations of titania nanotubes, the structure becomes highly disordered, resulting in longer electron pathways, which degrade the overall transport properties of the electrode. Ghadiri et al. [48] proposed a hollow nanofiber PA morphology, which has transport properties superior to those based on nanoparticles, because the nanofibers have a lower number of contact points and hence a less tortuous electron path and a lower number of traps. Since the quality of the contact points between nanostructures affects

the overall transport properties, nanospindles, having low-defect single-crystalline faceted surfaces, were synthesized, demonstrating better transport properties when used in DSSC PAs and improving the overall conversion efficiency [49].

Indeed, the trap-limited transport mechanism usually overwhelms the role of the structural order in the transport properties; thus, Villanueva et al. [93] proposed an approach to evidence the structural effects free from the interference of transport-limiting traps. To this end, they conveniently described the diffusion coefficient D as a function of the freely mobile electron diffusion coefficient D_0 by the relation [93]

$$D \sim D_0 \left(\frac{N}{N_C} \right)^{\left(\frac{1}{\alpha} - 1 \right)} \quad (3)$$

where α is a parameter describing the “energetic disorder” (related to the number of localized states in the band gap: i.e., the smaller is α the higher is the disorder), N is the total photoelectron density, and N_C is the effective density of trap states at the transport (mobility) edge. While D_0 is unaffected by the energetic disorder associated with the exponential distribution of band gap states and surface traps, it depends on the structural disorder, i.e., grain size, number and surface area of the particle boundaries. With the proposed approach, it is possible to determine the dependence of D_0 on the square of the particles’ size and demonstrate that the transport velocity can decrease by two orders of magnitude from a bulk situation, with D_0 ranging between 0.1 and 0.5 cm² s^{−1} (when the particle size tends to the micrometer film thickness value) to small nanoparticles, with $D_0 \approx 10^{-3}$ cm² s^{−1} (diameter down to few nanometers), while trapping effects can have an impact up to five orders of magnitude on the transport time. This observation shows the necessity of the development of high-quality crystalline structures, where direct electron pathways, enabling good transport properties (with the high specific surface area necessary for high dye load), allow highly efficient energy conversion, which is even more relevant in low illumination conditions, such as in indoor applications.

For this purpose, hierarchical nanostructures, constituted by long nanotubes or nanowires, decorated with nanoparticles or nanobranched, were therefore synthesized and used as mesoporous PA in DSSCs [44,94–97]. Results reported by Qu et al. [94] demonstrated that, with respect to PAs based on nanoparticles, those made of hierarchical structures showed improved charge transport properties, due to the low trap density in the highly crystalline structure and short electron path (see Figure 5), but also the specific surface area was still low and needed to be optimized for the generation of high current density. On the other hand, Wu et al. [46] demonstrated that processes leading to the formation of small nanobranched on nanorod structures, even if producing high surface area PA with a high short circuit photocurrent, deteriorate the charge transport properties, inducing the formation of a large number of defects. Thus, even if the use of hierarchical structures paved the way for high efficiency DSSCs, the optimization of the functional properties of the mesoporous films is still necessary for their practical exploitation.

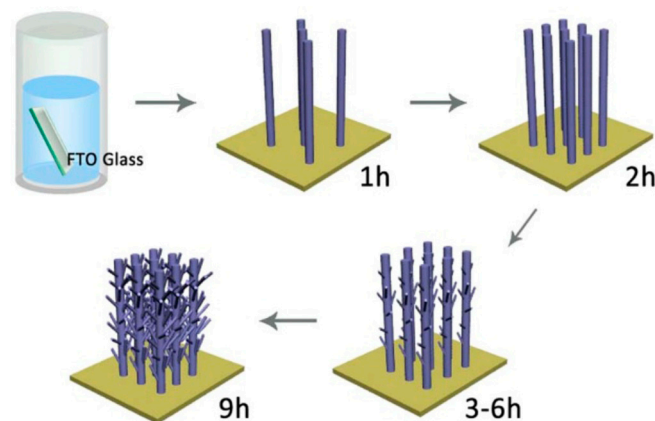


Figure 5. Schematic of formation process of hierarchical TiO_2 nanostructures. Reproduced from 354 Reference [97] under the Creative Commons CC-BY-NC-ND license.

As discussed above, the high absorption coefficient of the perovskites reduces the necessary PA thickness in PSCs down to a range between 400 nm and 1.5 μm [96]; this small thickness value immediately relaxes the requirements for the charge transport properties in the titania layer. Nevertheless, the morphology of the TiO_2 film strongly influences the overall performance of PSCs. It was indeed demonstrated that the porosity of the titania scaffold, which mainly depends on the dimensions of spherical nanoparticles, determines both the perovskite coverage and crystallinity [98–103]. Improved coverage of the titania scaffold, obtained by increasing the porosity, gives rise to better light harvesting capabilities and hence results in higher short circuit current density generation [101,102,104]. Another consequence of the improvement of the TiO_2 scaffold coverage is the reduction of undesired electron–hole recombination, which occurs at the interface between electron and hole-transport layers; accordingly, a more effective capability of charge extraction from the perovskite was demonstrated by measuring the photoluminescence intensity, which decreases for increased titania film porosity while maintaining the same thickness. It was also reported that when maintaining the same morphology, when the titania film thickness exceeds an optimal value, the transport characteristics of the electrode [104] degrade because the perovskite coverage decreases, allowing recombination processes, and also, as widely discussed above, the number of interparticles connections decreases, lengthening the electron path. Moreover, many papers report on the impact of the perovskite grain size on the charge recombination processes not explicitly addressing the role of the titania scaffold morphology [100,105,106] but showing the improved performance of cells with larger grains, which are less affected by trap-assisted recombination at the grain boundaries.

Aside from the interest in the optimization of titania scaffolds based on spherical nanoparticles, many papers report on the performance achieved with completely different nanostructures. On one hand, the nanotubes and nanorods ordered structures that, while being unsuitable as dye-sensitized PA with submicrometer thickness for the low surface area (and hence low dye load), were demonstrated to allow good performance when used as a perovskite scaffold [107–111]. On the other hand, a wide variety of mesoporous films created by disordered nanowires and nanofibers [112,113] or even hierarchical heterostructures [114–116] showed good performance in PSCs.

The results presented in this review represent the evolution and the latest progress related to the use of titania mesoporous films in dye-sensitized and perovskite solar cells. However, research is still in progress in both the fields because of the high expected impact that their commercialization would have on the sustainable production of energy. Indeed, thanks to their high conversion efficiency under dim light (up to 32%) [23–25], DSSCs are promising devices to recycle the consumed electric power in indoor applications; on the other hand, the high conversion efficiency demonstrated by PSCs paves the way for their commercialization for high-power photovoltaic plants. Moreover, the capability of both DSSCs and PSCs to be implemented in thin flexible modules [117,118] with a pleasant

aesthetic appearance makes them the ideal candidates for both portable electronics and building-integrated photovoltaics [4,119].

3. Photoelectrochemical Water Splitting

One of the most studied applications of nanophase TiO₂ in green energy production is its use as a photoanode for hydrogen generation through the light-driven decomposition of water in a photoelectrochemical (PEC) device [120–123].

Titanium dioxide presents many of the characteristics of an ideal semiconductor, such as chemical and biological inertia, photocatalytic stability and ease of production. Moreover, it is cheap and free of risks to human health and the environment; noticeably, for PEC applications, the most important drawback of TiO₂ is that it can be activated only by ultraviolet light, so only about 4% of the solar spectrum can be used in solar-driven generators. In fact, photoexcitation of TiO₂ occurs when the impinging photon energy is greater than the semiconductor bandgap, which is equal to 3.2 eV and 3.0 eV for the two most common crystalline phases of pure TiO₂, i.e., anatase and rutile, respectively. Given the focus of this review on morphology, we do not discuss here the most studied strategies adopted to develop visible light responsive photocatalysts, such as doping or modification of the surface with plasmonic nanostructures or dyes [124–127]; instead, we show how the optical efficiency can be improved by exploiting light-trapping effects, referring to the theoretical background given in the previous section.

When immersed in water, TiO₂ is very stable, and its photoexcitation can drive a redox process in the interfacial region between the fluid and the semiconductor, since the electron-hole (e[−]/h⁺) pair that is created is energetically rich and can activate chemical reactions according to the following paths:



Separation of the photogenerated e[−]/h⁺ pairs occurs in the semiconductor because of the electric space-charge field associated with the band-bending, which depends on the presence of surface states and the difference between the redox potential of the electrolyte and the Fermi level of the semiconductor [128,129]. The energetic holes, transported at the semiconductor surface, can effectively participate in the water oxidation reaction with consequent dissociation and hydrogen/oxygen evolution [1,130,131]; see Figure 6.

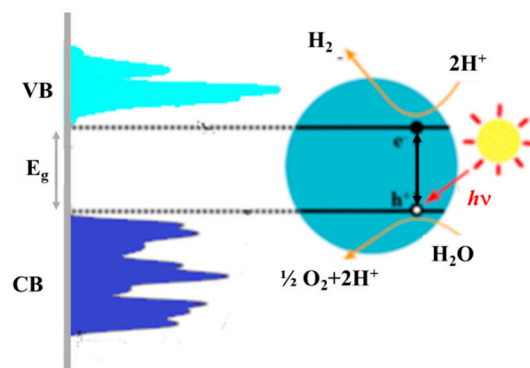


Figure 6. Scheme of the key steps of the photocatalytic reaction in a titania nanoparticle. If the incoming photon has an energy $h\nu$ greater than the value of E_g (energy gap or band gap), an electron (e[−]) can be promoted from the valence band (VB) to the conduction band (CB), leaving behind a hole (h⁺). The electronic structures of VB and CB were determined from X-ray Absorption and Emission Spectroscopy. Adapted with permission from [132]. Copyright 2014, American Chemical Society.

Photoinduced hydrogen production from water splitting can also be obtained in a PEC cell, where the main components are the semiconductor light-absorbing photoanode, the water-based electrolyte and the cathode (see Figure 7) [133], this process being more interesting for long-term applications with respect to the photocatalytic operation, as it provides gas separation and post-operation material recovery.

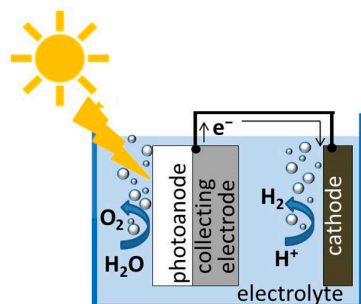


Figure 7. Schematics of a photoelectrochemical cell for water-splitting. The light impinging on the photoanode generates hole and electron pairs; the first migrate to the surface and promote the oxygen evolution, while the second, after travelling to the cathode, drive the hydrogen evolution.

In the PEC cell described above, three major physicochemical steps are involved [134]. The first step is the light absorption by the semiconducting (n-type) photoanode, i.e., TiO_2 in our case of interest, which produces pairs of charge carriers; the second step is the separation and transportation [135] of the photogenerated pairs: electrons travel through the photoanode to the collecting electrode contact, while holes travel towards the electrode/electrolyte interface. The last step consists of the surface redox reactions at the electrodes, namely water oxidation (reaction 4.2) at the photoanode and proton reduction (reaction 4.3) at the cathode, resulting in water splitting. An efficiency parameter can be related to each of these three steps so that the overall efficiency, $\eta_{overall}$, of PEC water splitting can be expressed as [136]

$$\eta_{overall} = \eta_{e^-/h^+} \cdot \eta_{transport} \cdot \eta_{interface} \quad (5)$$

where η_{e^-/h^+} is the efficiency of e^-/h^+ photogeneration, $\eta_{transport}$ is the efficiency of charge transport, and $\eta_{interface}$ is the efficiency of surface reactions. Experimentally, to evaluate the performance of a PEC PA, the most common practice is to measure the photocurrent under illumination, because it is proportional to the hydrogen or oxygen production rate [123]. Indeed, the solar-to-hydrogen conversion efficiency is proportional to the photocurrent circulating in the external circuit according to the relation [123]

$$\eta_{overall} = \frac{V_{redox} J}{P} \quad (6)$$

where J is the photocurrent density (in A m^{-2}), P is the power density of illumination (in W m^{-2}), and V_{redox} is the potential corresponding to the Gibbs free energy change per photon required to split water (which is equal to 1.23 V).

Since the first PEC cell with a TiO_2 PA was assembled [130], the search for materials and experimental conditions that better fulfill the thermodynamic and kinetic requirements for efficient water splitting photoconversion has been underway. In this respect, nanostructured electrodes present undoubted advantages. The first benefit is due to the capability of nanostructures to improve the coupling with incoming photons by LT, eventually producing an optical absorption enhancement (see Section 2.1); the second is the possibility of decoupling the direction of light absorption and charge-carrier collection; that is, instead of diffusion through the bulk material, orthogonal separation of photogenerated charges occurs, and the probability of charge recombination is reduced [137]; finally, the third advantage achieved by nanostructuring is the huge increase of the surface area [138,139]

that, enlarging the number of reaction sites [140], improves $\eta_{interface}$. In the following, in line with the scope of this review, we discuss how titania morphology and structure impact the functionality of the electrodes in PEC devices and report the main published experimental results.

3.1. Light Management

Following the photon absorption process, the carrier photogeneration efficiency η_{e^-/h^+} is expected to increase with the TiO₂ film thickness, until this is within the effective region of photon penetration, which spans from ≈ 0.3 to 10 μm in the UV region from 330 nm to 370 nm depending on the photon wavelength [141]. In the visible part of the solar spectrum, titania is only slightly absorbing, so, as in the photovoltaic applications (see Section 2.1), LT occurring in the nanostructured electrode can be exploited to enhance absorption with the ultimate effect of improving the conversion efficiency under solar irradiation. In water splitting applications, only few papers report on light management strategies adopted to improve the performance of PEC cells. In particular, Ibadurrohman et al. [135] studied the behavior of PEC cells based on mesoporous electrodes made of nanoparticles and attributed part of the conversion efficiency improvement to the surface roughness induced by the use of a PEG template in the synthesis of the titania film, even though they could not disentangle LT effects from charge separation and transport ones. More explicitly, Qiu et al. [142] discussed, in terms of LT within the mesoporous structure, the higher conversion efficiency in electrodes made of hierarchically branched anatase TiO₂ nanotetrapods with respect to nanoparticles-based ones, showing that the former structure has better light diffusing properties (see Figure 8). The improved efficiency due to the occurrence of LT when using 1D structures is also reported in Yu et al. [143], Shankar et al. [144] and Ozkan et al., who pointed out the role of the interspacing of TiO₂ nanotubes (tube-to-tube spacing) in the light diffusion process [145].

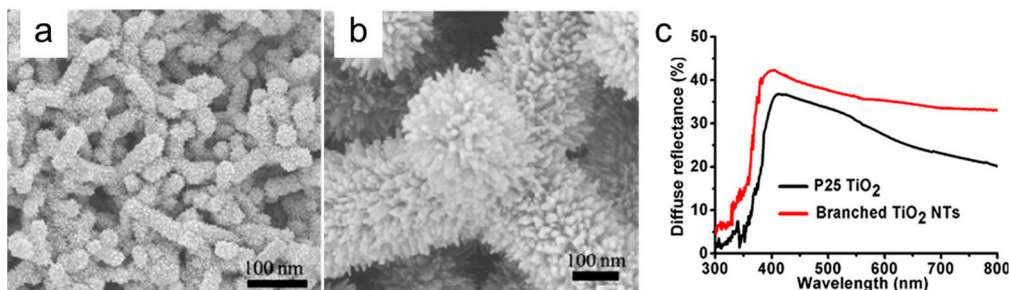


Figure 8. SEM images of hierarchical titania nanostructures (a,b), and diffuse reflectance spectra (c) of electrodes made of commercial titania nanoparticles (black curve) and of hierarchical nanostructures (red curve). Adapted with permission from [142]. Copyright 2014, American Chemical Society.

In addition, as outlined for PSCs (see Section 2.1), a nanostructured interface between the collecting electrode and the titania film was demonstrated to efficiently trap solar radiation; in [142], aluminum nanospikes were created on the TCO surface, while Chiarello et al. [146] showed that ordered titania nanotubes in a photonic crystal structure confine light of a selected wavelength in the region of the walls, exploiting the periodical modulation of the refractive index to enhance the light absorption.

3.2. Surface Reactivity and Electron Transport

As already mentioned, the efficiency of surface reactions ($\eta_{interface}$) is strictly linked to the number of reaction sites and the PA surface area. The simplest and in principle most efficient strategy to enlarge the specific surface area of the PA is depositing small nanobeads (0D structures) on the collecting electrode [147,148]. This kind of film exhibits a huge increase in the specific surface area for decreasing particle diameter. In addition, the small nanoparticle dimension allows the photogenerated holes to reach the surface

with a very short travel distance, thus minimizing undesired recombination processes. Nevertheless, a minimum nanoparticle size (≈ 1 nm) is required because the photocatalytic activity decreases with decreasing size, as demonstrated by a theoretical study showing that the water splitting reaction in very small beads is thermodynamically disadvantaged because of the strong self-trapping of free electrons and holes [149]. Experimentally, it was demonstrated that maximum photocatalytic efficiency is obtained for particle dimension of about 25 nm [150], which is a trade-off between optical requirements (larger particles absorb light more efficiently) and the necessity of maximizing the ratio of the e^-/h^+ pairs at the interface to total generated ones (which increases as the particle size decreases).

As thick PAs are desirable to attain high photocurrent density and improve overall cell efficiency (because the number of reaction sites and the optical absorption grow), many efforts have been devoted to developing highly efficient PEC cells based on thick PAs. One of the main bottlenecks presented by thick films is constituted by the difficult access of the electrolyte to the pores through the whole electrode, so different strategies were adopted in the preparation of the film to control and optimize the porosity. In sol-gel methods, the addition of surfactant was used to control the pore (and titania crystallite) dimensions, achieving properly porous thick films (thickness up to ≈ 1.2 μm) with improved photocatalytic activity [151]. In spray pyrolysis preparation methods, highly porous and rough films were realized by using a templating agent (see Figure 9), attaining an improved conversion efficiency of a factor 5 [135] with respect to PAs made of unmodified titania beads. On the other hand, for electrosprayed films, the structure [152] is mainly determined by the nanoparticle aggregation in the starting suspension. For such kinds of electrodes, it was demonstrated that large pores are created by depositing large clusters. Nevertheless, a detrimental reduction of hydrogen generation for excessively porous films was observed [153,154]; this phenomenon can be attributed both to the long and tortuous path of the electrons, leading to undesired recombination processes, and also, as reported for DSSCs electrodes [155], to a tortuous path for ion diffusion. For this reason, a trade-off between high porosity, leading to high surface area and easy electrolyte access, and short electron (and ion) paths are necessary to reach a high hydrogen production rate.

Unlike what happens in a photocatalytic reactor, in a PEC cell, the fate of photogenerated holes and electrons is quite different: while the first, as in photocatalysis, only need to reach the nanoparticle surface to react with the electrolyte, electrons must travel to the collecting electrode through the nanostructured titania PA. Therefore, the hole diffusion length of about 10–70 nm measured in nanostructured TiO_2 [15,135,156–158] is quite sufficient to guarantee the hole transport efficiency close to unity, while the electron transport could represent a bottleneck for the overall hydrogen production efficiency [159]. Electron transport in mesoporous electrodes made of almost spherical nanoparticles has been widely studied in DSSCs, as reported in Section 2.2, and some papers demonstrated that, also in water-splitting PEC cells, the electron travel is random walk-like and subject to multiple trapping and detrapping events [80,141].

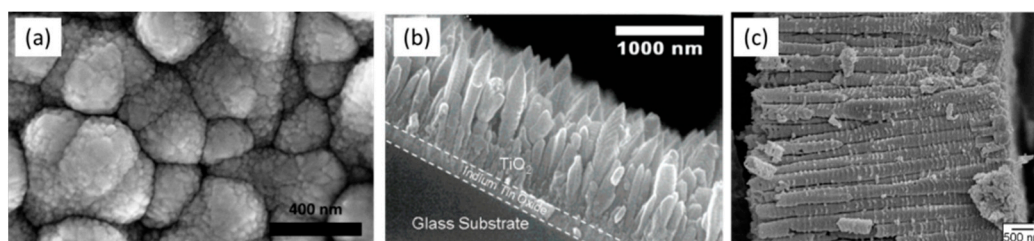


Figure 9. SEM images of different titania nanostructures for PEC electrodes: rough nanobeads (a) adapted with permission from [135], Copyright 2015, American Chemical Society, columnar (b) adapted with permission from [160], Copyright 2008, American Chemical Society, and tubular structures (c) adapted with permission from [144], Copyright 2009, American Chemical Society.

A useful parameter to quantify the competition between the diffusive transport and the recombination process is the electron diffusion length, which is the average displacement of an electron before recombination. In a PEC cell, the electron diffusion length of a nanoparticle-based PA was measured under illumination by UV light (wavelength between 330 and 390 nm), obtaining values ranging from 8.5 to 12.5 μm [141]. These experimental results showed that for electrode thicknesses up to a few micrometers, i.e., optimized for UV light harvesting, the electron collection is quite efficient. Nevertheless, thicker PAs are necessary to increase both the reactive area and the exploitation of the solar spectrum by extending light harvesting to visible, which is poorly absorbed in titania [141]; hence, when increasing the electrode thickness up to 10 micrometers or more, the requirements on the electron diffusion length become more severe.

To fulfil this necessity, so far, one-dimensional (1D) nanostructures (see Figure 9) such as columnar single crystals [160] nanotubes [161–163], nanowires [164–166], nanofibers [167–171] and nanorods [170,171] have been extensively studied for the superior electronic properties (longer charge carrier lifetimes and shorter transport times), as widely discussed in Section 2.2.

Lately, the most investigated morphology of nanostructured TiO_2 PAs is the tube-shaped one, vertically aligned with respect to the collecting electrode. In such kinds of electrodes, photogenerated holes only need to move radially across the nanotube wall to react at the solid/electrolyte solution interface, while the electrons follow the direct conduction pathways along the wall, improving the charge collection [172]. A great effort has been spent on the optimization of the morphology of nanotubes, since PEC tests showed that besides crystallinity, length, pore diameter and wall thickness critically affect photoelectrochemical activity [173,174]. Indeed, PAs made of nanotubes with small pore diameters exhibit low photocurrent, and the phenomenon is explained by the hindered diffusion of the electrolyte solution into the tubes [151,175–177] and the higher charge transfer resistance. As regards the wall thickness, thin-walled (3–5 nm) nanotubes facilitate the diffusion of the photogenerated holes to the semiconductor/electrolyte interface during water splitting, allowing for efficient separation of charges [145,176]; also, porous-wall nanotubes were used in PEC devices, showing a good photoconversion efficiency [178], thanks to the increased surface area.

Regarding the tube length, many papers report on the study of the optimal length to obtain a high PEC performance, but a wide consensus on this parameter is still missing due to discordant results, even though it is clear that a compromise between $\eta_{interface}$ and $\eta_{transport}$ is needed [175]. Generally speaking, the 1D nanostructuring is less effective than 0D for the increase of the specific surface area; so, if compared to electrodes made of 20 nm diameter beads, electrodes made of nanotubes (wall thickness 20 nm, inner diameter 10 nm) should be thicker by a factor of 2 to recover the same specific surface, but increasing the tube length affects electrolyte diffusion and enhances the requirements on conduction properties, although improving the light absorption at longer wavelengths. So, several works [179–181] have reported that the increase in TiO_2 tube length provides higher PEC activity by enlarging the active surface area, thus increasing the number of the reaction sites and also offering higher absorption of the incident light. In this direction, a remarkable photoconversion efficiency of 16.25% was achieved under UV illumination in a PEC with an electrode made of nanotube arrays long up to 30 μm with suitable wall crystallinity [182]. In other works, the photocurrent density was proven to decrease with increasing tube length, and the effect was explained in terms of the higher chances of the e^-/h^+ pair recombination for the longer paths. For instance, a significant decrease in photocurrent density was found when the nanotube length was higher than about 5 μm [179], while the highest performance (50 $\mu\text{A cm}^{-2}$) was recorded for nanotubes not longer than 2 μm [183] and 1 μm [161]. These discordant results can be ascribed to the different transport properties of the tubes, due for example to crystallinity, trap density and quality of the interface with the collecting electrode; all these characteristics are strictly related to the preparation process, which ultimately determines the optimal tube length. Thus, characterization protocols enabling

the disentanglement of the length on the functional behavior of the PA from the synthesis procedure and the direct comparison of the published results could greatly boost the optimization of novel electrodes.

To exploit the direct electron paths in 1D structures, while increasing the surface area, tubular TiO₂ PAs with additional branches grown out from the plate-like backbone structure have been studied (Figure 10). They present excellent charge separation and transport efficiency and also provide a highly accessible surface area, as the branches act as direct pathways to efficiently extract holes from the bulk structure to the semiconductor/electrolyte interface, which results in faster separation of photogenerated e⁻/h⁺ pairs and facilitates reactions at the semiconductor/electrolyte interface [184,185]. Moreover, the photogenerated electrons are transported efficiently via the single-crystalline backbone nanostructure as the direct pathways to counter electrodes for proton reduction. The use of this kind of structure leads to a high photocurrent of up to 1.02 mA cm⁻², which is close to the theoretical upper limit of photocurrent density of anatase TiO₂ (1.1 mA cm⁻²) [184,185]. Furthermore, it was argued that the direct growth of this nanostructure on TCO provides an intimate contact between the film and substrate and improves the electron collection efficiency [185].

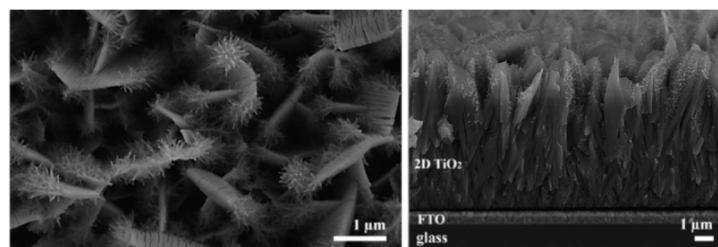


Figure 10. SEM images of branched tubular titania structures. Adapted with permission from [184], Copyright 2018, Wiley.

Other studies present an attractive alternative, building a hierarchically porous system joining macropores within the mesoporous films, which can lead to more accessible pore openings and increase the availability of the internal surface. PAs constituted of hierarchically macro/mesoporous TiO₂ films prepared by a template synthesis reveal excellent performance in PEC water-splitting due to a high surface area and hierarchical pores with 3D interconnected highly crystalline anatase frameworks [186].

Yang et al. [187] report 3D nanostructured hierarchically TiO₂ photoanodes characterized by a core-shell structure: these structures combine nanodendrites in a core portion and a shell portion formed by nanoparticles sequentially located on the surface. The inner TiO₂ array provides a fast electron transport pathway due to its quasi-single-crystalline structure, while the nanoparticles in the shell portion provide a larger surface area for more efficient charge separation without significantly sacrificing the electron collection efficiency. Furthermore, the combination of crystalline rutile and anatase phase in a 3D hierarchical structured PA shows a remarkable photocurrent density of 2.08 mA cm⁻² thanks to the combination of crystalline phases of rutile/anatase in the 3D structure (the maximum photocurrent for rutile TiO₂ at 1.23 V vs. reversible hydrogen electrode under simulated sun light at 100 mW/cm² was calculated to be 2 mA/cm²) [187].

Considering the current state, PEC technologies are still far from meeting the demand for successful industrialization. Nevertheless, the increasing global demand for sustainable and environmentally friendly energy production encourages further research on solar-driven hydrogen production. In particular, there is a large consensus on the benefits of both the development of novel nanophase photocatalysts and of new architectures of the heterojunction between TiO₂ and cocatalysts. Further studies are expected to overcome the main bottlenecks, such as low utilization of solar energy and high cost of synthesizing materials, paving the way for the scaling-up of the low-cost production of high performance devices.

4. Thermal Energy Management by Nanofluids

Nanofluids (NFs) are colloidal suspensions of nanoparticles (beads, nanofibers, nanotubes, etc.) dispersed in a base fluid, generally water, ethylene glycol or oil, where the nanophase has the function of modifying the thermal transport properties of the base fluid. Among all the nanoparticles with suitable thermal properties, including metallic and nonmetallic ones, TiO₂ nanoparticles are most commonly used, due to the stability of their chemical structure, their biocompatibility and their electrical, optical and physical properties [188–191].

NFs have attracted particular interest because of their capacity to increase heat transfer efficiency in coolant applications, showing higher thermal conductivity values than those predicted by the classical models for composites [192–196]. These models, derived from the Maxwell theory [197] for electrical conductivity of composites, are essentially based on the Effective Medium Approximation (EMA) [198–200] and describe stationary systems characterized by the conductivity of phase constituents (base fluid, k_l , and nanoparticles, k_p) and the nanoparticle volume fraction (φ_p), originally dealing with spherical inclusions. Later, in the Hamilton and Crosser (HC) model, ellipsoidal particles were included through the introduction of a sphericity parameter n [201] with values ranging from 3 to 6 for spherical to ellipsoidal particles; in this case, the effective thermal conductivity is expressed as

$$\frac{k}{k_l} = \frac{k_p + (n-1)k_l + (n-1)\varphi_p(k_p - k_l)}{k_p + (n-1)k_l - \varphi_p(k_p - k_l)} \quad (7)$$

Further refinements of the basic EMA model considered the contribution of the interfacial thermal resistance (R_b) between the composing phases for spherical and ellipsoidal particles [202,203]. Indeed, although R_b can be considered negligible for microsized particles, for nanosized inclusions, its impact should be pronounced due to the larger surface area, which leads to a reduction in the thermal conductivity of the composite system [204]. On the other hand, Wilson et al. [205] and Huxtable et al. [206] experimentally measured the R_b between different nanoparticle/fluid couples, obtaining values ranging from $0.77 \cdot 10^{-8} \text{ Km}^2 \text{ W}^{-1}$ to $20 \cdot 10^{-8} \text{ Km}^2 \text{ W}^{-1}$. Compared with solid/solid interfaces, such low thermal resistance values cannot limit the heat transfer and affect the thermal conductivity in NFs [207].

Diversely, other theoretical approaches considered the particle/fluid system as a dynamic system, where the heat transport is favored by the convection mechanism induced by the Brownian movement (BM) of the nanoparticles [208–211]. For instance, Kumar et al. [212] extended the stationary model to include the effect of the nanoparticle motion in terms of particle velocity as responsible for the thermal conduction, demonstrating its key role in determining the temperature dependence of the heat conduction. Later, Prasher et al. [213] proposed a Brownian motion-based convective–conductive model to explain the behavior of the NFs with respect to temperature and nanoparticle concentration and size, even though some opposing results evidenced that the BM does not have much influence on thermal conduction [214–216].

Notwithstanding the numerous theoretical approaches present in the literature to predict the thermal conductivity enhancements measured in NFs, none can reproduce the observed thermal conductivity enhancements in the full achievable range of particle size and temperature, so this is a currently very active area of research.

Experimentally, for TiO₂-based NFs, different thermal conductivity enhancements with respect to the base fluid are reported in the literature: for instance, typical enhancements of 2–3% were observed at low nanoparticle volume fractions (<1%) [217–220] in similar temperature range and nanoparticle size conditions (10–30 nm), while other researchers measured larger thermal conductivity enhancements up to 20% [193,221]. Reasons for these discordant values can be traced both to the different experimental techniques used for the thermal characterization and, more interestingly, to the different NFs' physical and chemical characteristics [222,223]. As for the experimental techniques, for example, the

most common methods used to measure the effective thermal conductivity of nanoparticle suspensions, such as the transient hot-wire method [224], the steady-state parallel method [217,225], the temperature oscillation method [226] and the hot strip method [227], can influence the natural thermal convection of the base fluid by adding additional heating that can affect the measurement results. Diversely, the forced Rayleigh light scattering method [220,228,229] is a contact-free method with a very short measuring time that limits the temperature rise during the measurement, leaving the system conditions unaltered. On the other hand, as mentioned before, the reported thermal conductivity differences are also a result of different NF characteristics such as nanoparticle dimensions and morphology, polydispersity, volume fraction and the presence and structure of aggregates, but also the base fluid pH value, which, for instance, influences the particle clustering [230–232] and/or the liquid layering at the nanoparticle/liquid interphase [202,203,233–235], significantly modifying the thermal conduction.

In this section, we report recent and significant results on NFs based on titania nanoparticles dispersed in water, focusing our interest on the effect of the nanoparticle aggregate structure on the thermal conductivity enhancement. Indeed, in such systems, much experimental evidence shows that a diffusion-limited colloid aggregation process [236,237] occurs, leading to the formation of fractal nanoparticle aggregates, which can be described as being composed of the primary backbone structure of linear chains plus a secondary structure of side chains (dead ends) [236,237]. To model the thermal conductivity of such fractal aggregates, Prasher et al. [231] proposed a three-level homogenization model, schematized in Figure 11, where the conductivity is calculated by considering the backbone immersed in a medium with an effective conductivity given by the contribution of the dead ends immersed in the liquid matrix.

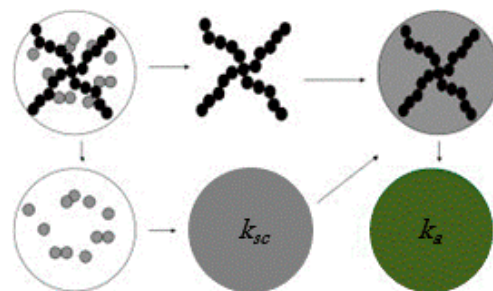


Figure 11. Schematic picture of the aggregate structure formed by nanoparticles arranged in a linear chain (black) and sidechains (gray). The conductivity of the whole aggregate (k_g) is calculated by considering the conductivity of the backbone nanoparticles embedded in a medium with an effective conductivity k_{sc} , due to the surrounding presence in the fluid of the sidechain nanoparticles. Adapted with permission from [231], Copyright 2006, AIP Publishing.

In [231], the contribution of dead ends k_{sc} is calculated using the Bruggeman model based on the EMA [202], which gives

$$\frac{(1 - \varphi_{sc})(k_l - k_{sc})}{(k_l + 2k_{sc})} + \frac{\varphi_{sc}(k_p - k_{sc})}{(k_p + 2k_{sc})} = 0 \quad (8)$$

where k_l and k_p are the thermal conductivities of the fluid and particle, respectively, and φ_{sc} is the volume fraction of particles belonging to dead ends, related to the volume fraction of particles in the aggregate φ_{in} and in the backbone linear chains and φ_{lc} by

$$\varphi_{sc} = \varphi_{in} - \varphi_{lc} \quad (9)$$

According to the general description of fractal aggregates, these quantities can be calculated from

$$\varphi_{in} = \left(\frac{R_a}{r_p} \right)^{d_f - 3} \quad (10)$$

and

$$\varphi_{lc} = \left(\frac{R_a}{r_p} \right)^{d_l - 3} \quad (11)$$

where d_f and d_l are the so-called fractal dimension and chemical dimension of the aggregate, respectively, R_a is the gyration radius (i.e., the radius of the embedding sphere), and r_p is the radius of the nanoparticles (here assumed spherical). The fractal dimension and the chemical dimension specify the geometry of the aggregate: d_f changes from 1 when all the nanoparticles are organized in a linear structure to 3 for spherical aggregates. In the case of TiO₂ nanoparticles dispersed in water, d_f has been measured to be in the range from 1.7 to 2.5 [238]. Analogously, the chemical dimension d_l ranges from 1, when all the nanoparticles are structured in side chains, to d_f , in which case all the nanoparticles are arranged in the backbone.

The thermal conductivity of the aggregate as a whole can now be calculated using a model developed for randomly oriented cylindrical particles [204] representing the backbone linear chains immersed in the effective medium due to the side chains, giving

$$k_a = k_{sc} \frac{3 + \varphi_{lc} [2\beta_{11}(1 - L_{11}) + \beta_{33}(1 - L_{33})]}{3 - \varphi_{lc} [2\beta_{11}L_{11} + \beta_{33}L_{33}]} \quad (12)$$

where L_{ii} and β_{ii} are geometrical factors strictly depending on the aspect ratio and on the thermal conductivities of the side chain nanoparticles and the base fluid [204]. Finally, the NF thermal conductivity k is calculated with the Maxwell-Garnett model [200] using the whole aggregate conductivity (12) and the volume fraction φ_a :

$$\frac{k}{k_l} = \frac{(k_a + 2k_l) + 2\varphi_a(k_a - k_l)}{(k_a + 2k_l) - \varphi_a(k_a - k_l)} \quad (13)$$

The introduction in the model of terms relative to different structural nanoparticle arrangements allows us to better predict the experimental thermal conductivity enhancements than other models accounting for the aggregation effects [232,239]. Indeed, the data reported in Figure 12, obtained by expression (13), based exclusively on the conduction mechanism, show that spherical aggregates appear to be detrimental to the thermal conductivity enhancement, while linear chained structures, providing preferential conduction paths (percolation effect), promote the thermal conductivity enhancements with values over 10% [230,240,241].

The overall thermal conductivity of NFs based on fractal aggregates expressed by relation (13) was also validated by Prasher et al. [231] using Monte Carlo (MC) simulations. The large predicted difference of about 12% between the thermal conductivity enhancements of fractal aggregates compared to well-dispersed nanoparticles confirmed the strong effect of the structure (in terms of fractal and chemical dimensions) and size of the aggregates on the thermal conduction.

The effective role of the aggregate structure on heat conduction was experimentally demonstrated by Philip et al., who used a colloidal suspension of magnetically polarizable Fe₂O₃ nanoparticles [242]. This work showed that, when an external magnetic field induced linear chain aggregation of the nanoparticles in the fluid, an extraordinary thermal conductivity enhancement (300%) was observed at a low nanoparticle volume fraction (0.2%). In titania NFs, with the same nanoparticle volume fraction, the presence of linear aggregates was demonstrated to increase the thermal conductivity up to 5%. The model proposed by Prasher et al. [231] was successfully used to interpret the thermal conductivity enhancements from 2% to 6%, measured by varying the nanoparticle volume fraction from

0.1% to 0.6% [220], using a fractal dimension equal to 2.1, which is in good agreement with other results obtained for same aggregates [243,244].

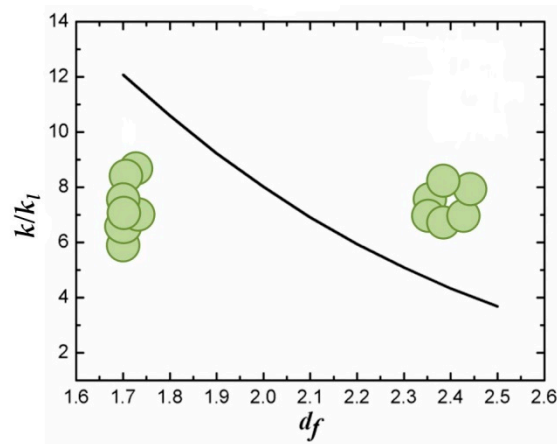


Figure 12. Influence of the fractal dimension on the thermal conductivity enhancement in TiO₂-based NFs using Equation (13) and the parameters described in [220]. Adapted with permission from [220], Copyright 2014, Wiley and Sons.

Many studies have shown that the aggregate structure is influenced by different factors (drivers), generally related to the NF's preparation parameters and to the temporal evolution of the aggregation state occurrences. For example, an optimum sonication time was found to induce the formation of small aggregates with linear structures and hence obtain a maximum thermal conductivity enhancement [245–248]. On the other hand, another way to induce the formation of linear chains of nanoparticles is to vary the pH value [190,248,249]. Although most of the experiments on thermal conduction reported in the literature were conducted at pH values ranging from 7 to 9 [246], a huge thermal conductivity enhancement of 20% was observed near the isoelectric point (pH = 4.5 in water) [248] in NFs containing 3% of TiO₂ volume fraction. At this pH value, the repulsive forces of the nanoparticles are absent, and the particles come closer due to van der Waals interactions, forming irregular aggregates with linear structures, thus improving the heat conduction. On the other hand, the aggregate mass increase can cause a drastic reduction of the measured thermal conductivity for the precipitation of the aggregates. To overcome the problem of the aggregates' sedimentation and to improve the stability of the NF, it is possible to modify the surfaces of the nanoparticles with different surfactants. In this way, greater stability of the NF and similar thermal conductivity enhancements at low nanoparticle volume fractions (<0.5%) were obtained when compared to unmodified nanoparticles [250–252], while at higher particle concentrations, the presence of surfactants leads to a significant enhancement in thermal conductivity, minimizing the formation of large spherical aggregates [251,253].

All the experimental results reported above were obtained at room temperature and generally deviated from the theoretical predictions here described within errors ranging from ±3% to ±5% [240]; however, when the experimental temperature was raised to 70 °C, larger deviations were observed [254,255]. To account for the temperature effects, Kundan et al. [240] introduced a term describing the micro-convection contribution induced by the nanoclusters' Brownian motion (BM) in Equation (13), obtaining

$$\frac{k}{k_l} = \frac{(k_a + 2k_l) + 2\varphi_a(k_a - k_l)}{(k_a + 2k_l) - \varphi_a(k_a - k_l)} \left(1 + AR_{eB}^m P_r^{0.333} \varphi_a\right) \quad (14)$$

where A and m are parameters whose values depend on the nature of the NF (for metal oxide $A \approx 5 \times 10^4$ and $m \approx 2.5\%$) [231,256], P_r is Prandtl's number [254], and R_{eB} is the Brownian Reynold number [257,258] accounting for the base fluid state, nanoparticles and fluid density and size. Equation (14) predicts that the contribution of the BM of the aggregates to the thermal conductivity enhancement at room temperature is limited,

while it becomes significant when increasing the temperature up to 70 °C because of the nanocluster's thermal excitations and, in some cases, for the breaking of large clusters into smaller ones.

Despite the different measurement conditions used, many experimental investigations on titania NFs showed an evident increase in the thermal conductivity enhancement when varying the temperature from 20 °C to 70 °C [190,240,250,259–261], in accordance with these predictions. Nevertheless, there is no unanimous agreement on the temperature dependence of the thermal conductivity, as demonstrated by Duangthongsuk et al. [262], who observed a decrease with the temperature rise, and by Turgut et al. [219], who showed a constant behavior.

Although in most of the published studies on NFs, the size of TiO₂ nanoparticles ranges from 20 to 40 nm, several works have indicated that at the same NF status and composition (base fluid, pH, temperature, nanoparticle volume fraction), the nanoparticle size impacts the NF thermal conductivity. In fact, very small particles (<10 nm) tend to aggregate, forming large compact clusters [263,264], which as predicted by Equation (13) leads to a reduction of the thermal conductivity enhancement, limiting the contribution of the BM to the heat transport [231]. On the other hand, in the presence of these small particles, at a volume fraction higher than 1%, the nanoaggregate–fluid interface plays a significant role due to the possible formation of a well-defined ordered layer with a solid-like structure (nanolayer) [235,265–268]. For this reason, Feng et al. [235] proposed a model combining the effects of the nanolayer's and nanoaggregate's presence on the heat conduction, considering the role of nanoparticle size and volume fraction, the thickness of the interfacial nanolayer, the thermal conductivities of the cluster and the base fluid. The model predictions are reasonable and in good agreement with the available experimental data on different metal oxide-based NFs.

The significant role of linearly structured aggregates on the thermal conduction mechanisms is also reflected in the large thermal conductivity enhancements observed in NFs containing non-spherical shape titania nanoparticles. Indeed, according to the HC model expressed by Equation (7), a higher thermal conductivity enhancement (about 3%) is predicted for rod-shaped titania nanoparticles compared to spherical ones [201]. However, some experimental evidence [269,270] reveals an even higher effect of nanoparticle shapes on thermal conduction than predicted. In particular, Murshed et al. [269] reported thermal conductivity enhancements of 20% for 1% rod-shaped (10 nm × 40 nm) nanoparticles volume fractions compared to 10% obtained for spherical ones (15 nm). To better interpret these high thermal conductivity enhancements obtained for particles with high aspect ratios, Wei et al. [271] proposed a new analytical expression based on the HC model, considering the effect of the aggregation and hence substituting the nanoparticle volume fraction and thermal conductivity with terms relative to the presence of fractal aggregates as described above. The comparison of their theoretical results with those obtained experimentally [269] showed a very good agreement, confirming the model's validity.

Accordingly, nanotubes should also provide an excellent model material for examining the effect of the particle shape on the thermal conduction of NFs [272–274]. However, despite the large thermal conductivity enhancements measured in carbon nanotube-based NFs [275,276], TiO₂ nanotubes dispersed in water showed lower values. For instance, Chen et al. [277] synthesized strongly protonated TiO₂ (titanate) nanotubes using the hydrothermal method [278] and observed a small thermal conductivity enhancement of about 3% with 0.6% nanotubes (10 nm × 100 nm) loading. Despite this small thermal conductivity enhancement, the measured values are higher than those predicted for well-dispersed non-spherical nanoparticles by the HC model and that observed in NF based on spherical nanoparticles. However, these results confirm the significant role of the nanoparticle shape on the thermal conduction enhancement; in particular, its crucial effect on the convective heat transfer and the clustering mechanism [277].

The results reported in this section highlight the significant role of the structure of fractal aggregates and the morphology of titania nanoparticles on the thermal conduction in

TiO₂-based NFs. Indeed, several experimental results showed that aggregates with a linear structure or nanoparticles with high aspect ratios could enhance thermal conductivity. In addition, among the numerous theoretical approaches present in the literature to interpret the high thermal conductivity enhancements observed experimentally, those based on the percolation effect due to the presence of fractal aggregates lead to the justification of the observed behavior of metal oxide-based NFs, especially with respect to the temperature and the nanoparticles' size and volume fraction dependence.

On the other hand, preparing NFs with a controlled size and structure of the aggregates is a crucial task and, due to difficulty in obtaining reproducible measurements, the experimental results are often controversial, making the interpretation of thermal mechanisms difficult.

Since the NFs are considered a valid alternative to simple fluids in many heat transfer applications, further and more accurate studies are required to better understand the role of the different NF parameters on heat transfer and to identify the mechanisms responsible for the thermal conductivity enhancement.

5. Conclusions

In this work, we reviewed three important applications of nanophase TiO₂ in the fields of energy production and management, with the scope of evidencing the importance of the material morphology and structure in optimizing the functional properties for each use. This approach allowed us to discuss in the same light photovoltaic energy conversion, hydrogen production by water splitting and thermal energy management by nanofluids. We reviewed the functionalities necessary for the use of the nanomaterial in each case, starting from the widely studied basic morphology, consisting of aggregated nanobeads, and arriving at 1D or hierarchical structures. Where possible, we described the models relating the nanomaterial properties to the process efficiency; notably, it appears that nanofluid modeling is the more developed field. Reasons for this might be related to the abundance of related studies on colloids and suspensions and also to the simpler functionality, i.e., thermal energy transport, required for the application. On the other hand, photovoltaics and water splitting applications could benefit from a unified modeling approach, which is however still lacking in the literature.

Author Contributions: Conceptualization, M.F.; investigation, M.F., S.G., F.R. and C.P.; resources, S.G., F.R. and C.P.; writing—original draft preparation, M.F., S.G., writing—review and editing, M.F., S.G., F.R. and C.P.; supervision, M.F. All authors have read and agreed to the published version of the manuscript.

Funding: This research received no external funding.

Institutional Review Board Statement: Not applicable.

Data Availability Statement: This study did not report any original data.

Conflicts of Interest: The authors declare no conflict of interest.

References

1. Chen, X.; Mao, S.S. Titanium Dioxide Nanomaterials: Synthesis, Properties, Modifications, and Applications. *Chem. Rev.* **2007**, *107*, 2891–2959. [[CrossRef](#)] [[PubMed](#)]
2. Akakuru, O.U.; Iqbal, Z.M.; Wu, A. TiO₂ Nanoparticles: properties and applications. In *TiO₂ Nanoparticles*; John Wiley & Sons, Ltd.: New York, NY, USA, 2020; pp. 1–66. [[CrossRef](#)]
3. Lan, Y.; Cook, L.; Lisfi, A. New Applications of TiO₂ Nanoparticles in Renewable Energy. In *Titanium Dioxide Nanoparticles: Characterizations, Properties and Syntheses*; NOVA Science Publisher: Hauppauge, NY, USA, 2017; p. 241.
4. Kokkonen, M.; Talebi, P.; Zhou, J.; Asgari, S.; Soomro, S.A.; Elsehrawy, F.; Halme, J.; Ahmad, S.; Hagfeldt, A.; Hashmi, S.G. Advanced Research Trends in Dye-Sensitized Solar Cells. *J. Mater. Chem. A* **2021**, *9*, 10527–10545. [[CrossRef](#)] [[PubMed](#)]
5. Ijaz, M.; Zafar, M. Titanium Dioxide Nanostructures as Efficient Photocatalyst: Progress, Challenges and Perspective. *Int. J. Energy Res.* **2021**, *45*, 3569–3589. [[CrossRef](#)]
6. Madian, M.; Eychmüller, A.; Giebel, L. Current Advances in TiO₂-Based Nanostructure Electrodes for High Performance Lithium Ion Batteries. *Batteries* **2018**, *4*, 7. [[CrossRef](#)]

7. Tian, X.; Cui, X.; Lai, T.; Ren, J.; Yang, Z.; Xiao, M.; Wang, B.; Xiao, X.; Wang, Y. Gas sensors based on TiO₂ nanostructured materials for the detection of hazardous gases: A review. *Nano Mater. Sci.* **2021**, *3*, 390–403. [[CrossRef](#)]
8. Bertel, L.; Miranda, D.A.; García-Martín, J.M. Nanostructured Titanium Dioxide Surfaces for Electrochemical Biosensing. *Sensors* **2021**, *21*, 6167. [[CrossRef](#)]
9. Amri, F.; Septiani, N.L.W.; Rezki, M.; Iqbal, M.; Yamauchi, Y.; Golberg, D.; Kaneti, Y.V.; Yulianto, B. Mesoporous TiO₂-Based Architectures as Promising Sensing Materials towards next-Generation Biosensing Applications. *J. Mater. Chem. B* **2021**, *9*, 1189–1207. [[CrossRef](#)] [[PubMed](#)]
10. Rehman, F.U.; Zhao, C.; Jiang, H.; Wang, X. Biomedical Applications of Nano-Titania in Theranostics and Photodynamic Therapy. *Biomater. Sci.* **2015**, *4*, 40–54. [[CrossRef](#)]
11. Rajaraman, T.S.; Parikh, S.P.; Gandhi, V.G. Black TiO₂: A Review of Its Properties and Conflicting Trends. *Chem. Eng. J.* **2020**, *389*, 123918. [[CrossRef](#)]
12. Zhu, T.; Gao, S.-P. The Stability, Electronic Structure, and Optical Property of TiO₂ Polymorphs. *J. Phys. Chem. C* **2014**, *118*, 11385–11396. [[CrossRef](#)]
13. Low, I.-M.J. Rutile: Properties, Synthesis and Applications; Rutile: Properties, Synthesis and Applications. In *Rutile: Properties, Synthesis and Applications; Rutile: Properties, Synthesis and Applications*; NOVA Science Publisher: Hauppauge, NY, USA, 2020; p. 240.
14. Manzoli, M.; Freyria, F.S.; Blangetti, N.; Bonelli, B. Brookite, a Sometimes under Evaluated TiO₂ Polymorph. *RSC Adv.* **2022**, *12*, 3322–3334. [[CrossRef](#)]
15. Zhang, J.; Zhou, P.; Liu, J.; Yu, J. New Understanding of the Difference of Photocatalytic Activity among Anatase, Rutile and Brookite TiO₂. *Phys. Chem. Chem. Phys.* **2014**, *16*, 20382–20386. [[CrossRef](#)] [[PubMed](#)]
16. Niu, B.; Wang, X.; Wu, K.; He, X.; Zhang, R. Mesoporous Titanium Dioxide: Synthesis and Applications in Photocatalysis, Energy and Biology. *Materials* **2018**, *11*, 1910. [[CrossRef](#)]
17. Gerischer, H.; Willig, F. Reaction of Excited Dye Molecules at Electrodes. In *Physical and Chemical Applications of Dyestuffs*; Topics in Current Chemistry; Schäfer, F.P., Gerischer, H., Willig, F., Meier, H., Jahnke, H., Schönborn, M., Zimmermann, G., Eds.; Springer: Berlin/Heidelberg, Germany, 1976; pp. 31–84. [[CrossRef](#)]
18. Grätzel, M. (Ed.) *Energy Resources through Photochemistry and Catalysis*, 1st ed.; Academic Press: New York, NY, USA, 1983.
19. O'Regan, B.; Grätzel, M. A Low-Cost, High-Efficiency Solar Cell Based on Dye-Sensitized Colloidal TiO₂ Films. *Nature* **1991**, *353*, 737–740. [[CrossRef](#)]
20. Halme, J.; Vahermaa, P.; Miettunen, K.; Lund, P. Device Physics of Dye Solar Cells. *Adv. Mater.* **2010**, *22*, E210–E234. [[CrossRef](#)]
21. Amadelli, R.; Argazzi, R.; Bignozzi, C.A.; Scandola, F. Design of Antenna-Sensitizer Polynuclear Complexes. Sensitization of Titanium Dioxide with [Ru(Bpy)₂(CN)₂]₂Ru(Bpy(COO)₂)₂-. *J. Am. Chem. Soc.* **1990**, *112*, 7099–7103. [[CrossRef](#)]
22. Ren, Y.; Flores-Díaz, N.; Zhang, D.; Cao, Y.; Decoppet, J.-D.; Fish, G.C.; Moser, J.-E.; Zakeeruddin, S.M.; Wang, P.; Hagfeldt, A. Grätzel, M., Blue Photosensitizer with Copper(II/I) Redox Mediator for Efficient and Stable Dye-Sensitized Solar Cells. *Adv. Funct. Mater.* **2020**, *30*, 2004804. [[CrossRef](#)]
23. Freitag, M.; Teuscher, J.; Saygili, Y.; Zhang, X.; Giordano, F.; Liska, P.; Hua, J.; Zakeeruddin, S.M.; Moser, J.-E.; Grätzel, M.; et al. Dye-Sensitized Solar Cells for Efficient Power Generation under Ambient Lighting. *Nat. Photonics* **2017**, *11*, 372–378. [[CrossRef](#)]
24. Saeed, M.A.; Kang, H.C.; Yoo, K.; Asiam, F.K.; Lee, J.-J.; Shim, J.W. Cosensitization of metal-based dyes for high-performance dye-sensitized photovoltaics under ambient lighting conditions. *Dye Pigment.* **2021**, *194*, 109624. [[CrossRef](#)]
25. Saeed, M.A.; Yoo, K.; Kang, H.C.; Shim, J.W.; Lee, J.-J. Recent developments in dye-sensitized photovoltaic cells under ambient illumination. *Dye Pigment.* **2021**, *194*, 109626. [[CrossRef](#)]
26. Luque, A.; Hegedus, S. (Eds.) *Handbook of Photovoltaic Science and Engineering*, 2nd ed.; Wiley: Hoboken, NJ, USA, 2003; pp. 154–196.
27. Lee, M.M.; Teuscher, J.; Miyasaka, T.; Murakami, T.N.; Snaith, H.J. Efficient Hybrid Solar Cells Based on Meso-Superstructured Organometal Halide Perovskites. *Science* **2012**, *338*, 643–647. [[CrossRef](#)] [[PubMed](#)]
28. Redfield, D. Multiple-pass Thin-film Silicon Solar Cell. *Appl. Phys. Lett.* **1974**, *25*, 647–648. [[CrossRef](#)]
29. Yablonoitch, E. Statistical Ray Optics. *JOSA* **1982**, *72*, 899–907. [[CrossRef](#)]
30. Zhou, D.; Biswas, R. Photonic Crystal Enhanced Light-Trapping in Thin Film Solar Cells. *J. Appl. Phys.* **2008**, *103*, 093102. [[CrossRef](#)]
31. Usami, A. Theoretical study of application of multiple scattering of light to a dye-sensitized nanocrystalline photoelectrochemical cell. *Chem. Phys. Lett.* **1997**, *277*, 105–108. [[CrossRef](#)]
32. Usami, A. Theoretical Simulations of Optical Confinement in Dye-Sensitized Nanocrystalline Solar Cells. *Sol. Energy Mater. Sol. Cells* **2000**, *64*, 73–83. [[CrossRef](#)]
33. Shigenori, T. Performance Simulation for Dye-Sensitized Solar Cells: Toward High Efficiency and Solid State. *Jpn. J. Appl. Phys.* **2001**, *40*, 97–107.
34. Rothenberger, G.; Comte, P.; Grätzel, M. A contribution to the optical design of dye-sensitized nanocrystalline solar cells. *Sol. Energy Mater. Sol. Cells* **1999**, *58*, 321–336. [[CrossRef](#)]
35. Gagliardi, S.; Falconieri, M. Experimental Determination of the Light-Trapping-Induced Absorption Enhancement Factor in DSSC Photoanodes. *Beilstein J. Nanotechnol.* **2015**, *6*, 886–892. [[CrossRef](#)]

36. Ito, S.; Zakeeruddin, S.M.; Humphry-Baker, R.; Liska, P.; Charvet, R.; Comte, P.; Nazeeruddin, M.K.; Péchy, P.; Takata, M.; Miura, H.; et al. High-Efficiency Organic-Dye-Sensitized Solar Cells Controlled by Nanocrystalline-TiO₂ Electrode Thickness. *Adv. Mater.* **2006**, *18*, 1202–1205. [[CrossRef](#)]
37. Gao, F.; Wang, Y.; Shi, D.; Zhang, J.; Wang, M.; Jing, X.; Humphry-Baker, R.; Wang, P.; Zakeeruddin, S.M.; Grätzel, M. Enhance the Optical Absorptivity of Nanocrystalline TiO₂ Film with High Molar Extinction Coefficient Ruthenium Sensitizers for High Performance Dye-Sensitized Solar Cells. *J. Am. Chem. Soc.* **2008**, *130*, 10720–10728. [[CrossRef](#)] [[PubMed](#)]
38. Chiba, Y.; Islam, A.; Komiya, R.; Koide, N.; Han, L. Conversion Efficiency of 10.8% by a Dye-Sensitized Solar Cell Using a TiO₂ Electrode with High Haze. *Appl. Phys. Lett.* **2006**, *88*, 223505. [[CrossRef](#)]
39. Gálvez, F.E.; Kemppainen, E.; Míguez, H.; Halme, J. Effect of Diffuse Light Scattering Designs on the Efficiency of Dye Solar Cells: An Integral Optical and Electrical Description. *J. Phys. Chem. C* **2012**, *116*, 11426–11433. [[CrossRef](#)]
40. Agrios, A.G.; Cesar, I.; Comte, P.; Nazeeruddin, M.K.; Grätzel, M. Nanostructured Composite Films for Dye-Sensitized Solar Cells by Electrostatic Layer-by-Layer Deposition. *Chem. Mater.* **2006**, *18*, 5395–5397. [[CrossRef](#)]
41. Lee, K.-M.; Suryanarayanan, V.; Ho, K.-C. The Influence of Surface Morphology of TiO₂ Coating on the Performance of Dye-Sensitized Solar Cells. *Sol. Energy Mater. Sol. Cells* **2006**, *90*, 2398–2404. [[CrossRef](#)]
42. Huang, F.; Chen, D.; Zhang, X.L.; Caruso, R.A.; Cheng, Y.-B. Dual-Function Scattering Layer of Submicrometer-Sized Mesoporous TiO₂ Beads for High-Efficiency Dye-Sensitized Solar Cells. *Adv. Funct. Mater.* **2010**, *20*, 1301–1305. [[CrossRef](#)]
43. Koo, H.-J.; Kim, Y.J.; Lee, Y.H.; Lee, W.I.; Kim, K.; Park, N.-G. Nano-Embossed Hollow Spherical TiO₂ as Bifunctional Material for High-Efficiency Dye-Sensitized Solar Cells. *Adv. Mater.* **2008**, *20*, 195–199. [[CrossRef](#)]
44. Shao, W.; Gu, F.; Gai, L.; Li, C. Planar Scattering from Hierarchical Anatase TiO₂ Nanoplates with Variable Shells to Improve Light Harvesting in Dye-Sensitized Solar Cells. *Chem. Commun.* **2011**, *47*, 5046–5048. [[CrossRef](#)]
45. Wu, D.; Zhu, F.; Li, J.; Dong, H.; Li, Q.; Jiang, K.; Xu, D. Monodisperse TiO₂ Hierarchical Hollow Spheres Assembled by Nanospindles for Dye-Sensitized Solar Cells. *J. Mater. Chem.* **2012**, *22*, 11665–11671. [[CrossRef](#)]
46. Wu, D.; Wang, Y.; Dong, H.; Zhu, F.; Gao, S.; Jiang, K.; Fu, L.; Zhang, J.; Xu, D. Hierarchical TiO₂ Microspheres Comprised of Anatase Nanospindles for Improved Electron Transport in Dye-Sensitized Solar Cells. *Nanoscale* **2012**, *5*, 324–330. [[CrossRef](#)]
47. Chuangchote, S.; Sagawa, T.; Yoshikawa, S. Efficient Dye-Sensitized Solar Cells Using Electrospun TiO₂ Nanofibers as a Light Harvesting Layer. *Appl. Phys. Lett.* **2008**, *93*, 033310. [[CrossRef](#)]
48. Ghadiri, E.; Taghavinia, N.; Zakeeruddin, S.M.; Grätzel, M.; Moser, J.-E. Enhanced Electron Collection Efficiency in Dye-Sensitized Solar Cells Based on Nanostructured TiO₂ Hollow Fibers. *Nano Lett.* **2010**, *10*, 1632–1638. [[CrossRef](#)] [[PubMed](#)]
49. Qiu, Y.; Chen, W.; Yang, S. Double-Layered Photoanodes from Variable-Size Anatase TiO₂ Nanospindles: A Candidate for High-Efficiency Dye-Sensitized Solar Cells. *Angew. Chem. Int. Ed.* **2010**, *49*, 3675–3679. [[CrossRef](#)] [[PubMed](#)]
50. Nair, A.S.; Jose, R.; Shengyuan, Y.; Ramakrishna, S. A simple recipe for an efficient TiO₂ nanofiber-based dye-sensitized solar cell. *J. Colloid Interface Sci.* **2011**, *353*, 39–45. [[CrossRef](#)] [[PubMed](#)]
51. Zhu, K.; Neale, N.R.; Miedaner, A.; Frank, A.J. Enhanced Charge-Collection Efficiencies and Light Scattering in Dye-Sensitized Solar Cells Using Oriented TiO₂ Nanotubes Arrays. *Nano Lett.* **2007**, *7*, 69–74. [[CrossRef](#)] [[PubMed](#)]
52. Nakayama, K.; Kubo, T.; Nishikitani, Y. Electrophoretically Deposited TiO₂ Nanotube Light-Scattering Layers of Dye-Sensitized Solar Cells. *Jpn. J. Appl. Phys.* **2008**, *47*, 6610. [[CrossRef](#)]
53. Liu, Z.; Misra, M. Dye-Sensitized Photovoltaic Wires Using Highly Ordered TiO₂ Nanotube Arrays. *ACS Nano* **2010**, *4*, 2196–2200. [[CrossRef](#)] [[PubMed](#)]
54. So, S.; Kriesch, A.; Peschel, U.; Schmuki, P. Conical-Shaped Titania Nanotubes for Optimized Light Management in DSSCs Reach Back-Side Illumination Efficiencies > 8%. *J. Mater. Chem. A* **2015**, *3*, 12603–12608. [[CrossRef](#)]
55. Wu, W.-Q.; Huang, F.; Chen, D.; Cheng, Y.-B.; Caruso, R.A. Thin Films of Dendritic Anatase Titania Nanowires Enable Effective Hole-Blocking and Efficient Light-Harvesting for High-Performance Mesoscopic Perovskite Solar Cells. *Adv. Funct. Mater.* **2015**, *25*, 3264–3272. [[CrossRef](#)]
56. Jang, S.; Yoon, J.; Ha, K.; Kim, M.-C.; Kim, D.H.; Kim, S.M.; Kang, S.M.; Park, S.J.; Jung, H.S.; Choi, M. Facile fabrication of three-dimensional TiO₂ structures for highly efficient perovskite solar cells. *Nano Energy* **2016**, *22*, 499–506. [[CrossRef](#)]
57. Khan, J.; Rahman, N.U.; Khan, W.U.; Wang, Y.; Fu, S.; Ahmed, G.; Akhtar, M.N.; Wu, M. Hollow 3D TiO₂ sub-microspheres as an electron transporting layer for highly efficient perovskite solar cells. *Mater. Today Energy* **2021**, *19*, 100614. [[CrossRef](#)]
58. Ha, S.-J.; Heo, J.H.; Im, S.H.; Moon, J.H. Mesoscopic CH₃NH₃PbI₃ Perovskite Solar Cells Using TiO₂ Inverse Opal Electron-Conducting Scaffolds. *J. Mater. Chem. A* **2017**, *5*, 1972–1977. [[CrossRef](#)]
59. Kang, S.M.; Jang, S.; Lee, J.-K.; Yoon, J.; Yoo, D.-E.; Lee, J.-W.; Choi, M.; Park, N.-G. Moth-Eye TiO₂ Layer for Improving Light Harvesting Efficiency in Perovskite Solar Cells. *Small* **2016**, *12*, 2443–2449. [[CrossRef](#)]
60. Moon, B.C.; Park, J.H.; Lee, D.K.; Tsvetkov, N.; Ock, I.; Choi, K.M.; Kang, J.K. Broadband Light Absorption and Efficient Charge Separation Using a Light Scattering Layer with Mixed Cavities for High-Performance Perovskite Photovoltaic Cells with Stability. *Small* **2017**, *13*, 1700418. [[CrossRef](#)] [[PubMed](#)]
61. Choi, D.H.; Nam, S.K.; Jung, K.; Moon, J.H. 2D Photonic Crystal Nanodisk Array as Electron Transport Layer for Highly Efficient Perovskite Solar Cells. *Nano Energy* **2019**, *56*, 365–372. [[CrossRef](#)]
62. Haque, S.; Mendes, M.J.; Sanchez-Sobrado, O.; Águas, H.; Fortunato, E.; Martins, R. Photonic-Structured TiO₂ for High-Efficiency, Flexible and Stable Perovskite Solar Cells. *Nano Energy* **2019**, *59*, 91–101. [[CrossRef](#)]

63. Kim, D.I.; Lee, J.W.; Jeong, R.H.; Yu, J.-H.; Yang, J.W.; Nam, S.-H.; Boo, J.-H. Enhancing the Optical Properties Using Hemisphere TiO₂ Photonic Crystal as the Electron Acceptor for Perovskite Solar Cell. *Appl. Surf. Sci.* **2019**, *487*, 409–415. [[CrossRef](#)]
64. Zhong, J.-X.; Liao, J.-F.; Jiang, Y.; Wang, L.; Kuang, D.-B.; Wu, W.-Q. Synchronous Surface and Bulk Composition Management for Red-Shifted Light Absorption and Suppressed Interfacial Recombination in Perovskite Solar Cells. *J. Mater. Chem. A* **2020**, *8*, 9743–9752. [[CrossRef](#)]
65. Schwarzburg, K.; Willig, F. Origin of Photovoltage and Photocurrent in the Nanoporous Dye-Sensitized Electrochemical Solar Cell. *J. Phys. Chem. B* **1999**, *103*, 5743–5746. [[CrossRef](#)]
66. Solbrand, A.; Lindström, H.; Rensmo, H.; Hagfeldt, A.; Lindquist, S.-E.; Södergren, S. Electron Transport in the Nanostructured TiO₂–Electrolyte System Studied with Time-Resolved Photocurrents. *J. Phys. Chem. B* **1997**, *101*, 2514–2518. [[CrossRef](#)]
67. Koenenkamp, R.; Henninger, R.; Hoyer, P. Photocarrier Transport in Colloidal Titanium Dioxide Films. *J. Phys. Chem.* **1993**, *97*, 7328–7330. [[CrossRef](#)]
68. Hoyer, P.; Weller, H. Potential-Dependent Electron Injection in Nanoporous Colloidal ZnO Films. *J. Phys. Chem.* **1995**, *99*, 14096–14100. [[CrossRef](#)]
69. Cass, M.J.; Qiu, F.L.; Walker, A.B.; Fisher, A.C.; Peter, L.M. Influence of Grain Morphology on Electron Transport in Dye Sensitized Nanocrystalline Solar Cells. *J. Phys. Chem. B* **2003**, *107*, 113–119. [[CrossRef](#)]
70. Enright, B.; Fitzmaurice, D. Spectroscopic Determination of Electron and Hole Effective Masses in a Nanocrystalline Semiconductor Film. *J. Phys. Chem.* **1996**, *100*, 1027–1035. [[CrossRef](#)]
71. Benkstein, K.D.; Kopidakis, N.; van de Lagemaat, J.; Frank, A.J. Influence of the Percolation Network Geometry on Electron Transport in Dye-Sensitized Titanium Dioxide Solar Cells. *J. Phys. Chem. B* **2003**, *107*, 7759–7767. [[CrossRef](#)]
72. van de Lagemaat, J.; Benkstein, K.D.; Frank, A.J. Relation between Particle Coordination Number and Porosity in Nanoparticle Films: Implications to Dye-Sensitized Solar Cells. *J. Phys. Chem. B* **2001**, *105*, 12433–12436. [[CrossRef](#)]
73. Cao, F.; Oskam, G.; Meyer, G.J.; Searson, P.C. Electron Transport in Porous Nanocrystalline TiO₂ Photoelectrochemical Cells. *J. Phys. Chem.* **1996**, *100*, 17021–17027. [[CrossRef](#)]
74. Dloczik, L.; Ieperuma, O.; Lauermaann, I.; Peter, L.M.; Ponomarev, E.A.; Redmond, G.; Shaw, N.J.; Uhlendorf, I. Dynamic Response of Dye-Sensitized Nanocrystalline Solar Cells: Characterization by Intensity-Modulated Photocurrent Spectroscopy. *J. Phys. Chem. B* **1997**, *101*, 10281–10289. [[CrossRef](#)]
75. van der Zanden, B.; Goossens, A. The Nature of Electron Migration in Dye-Sensitized Nanostructured TiO₂. *J. Phys. Chem. B* **2000**, *104*, 7171–7178. [[CrossRef](#)]
76. Anta, J.A.; Ditrach, T.; Bisquert, J. Dynamics of Charge Separation and Trap-Limited Electron Transport in TiO₂. *J. Phys. Chem. C* **2007**, *111*, 13997–14000. [[CrossRef](#)]
77. van de Lagemaat, J.; Park, N.-G.; Frank, A.J. Influence of Electrical Potential Distribution, Charge Transport, and Recombination on the Photopotential and Photocurrent Conversion Efficiency of Dye-Sensitized Nanocrystalline TiO₂ Solar Cells: A Study by Electrical Impedance and Optical Modulation Techniques. *J. Phys. Chem. B* **2000**, *104*, 2044–2052. [[CrossRef](#)]
78. Kopidakis, N.; Schiff, E.A.; Park, N.-G.; van de Lagemaat, J.; Frank, A.J. Ambipolar Diffusion of Photocarriers in Electrolyte-Filled, Nanoporous TiO₂. *J. Phys. Chem. B* **2000**, *104*, 3930–3936. [[CrossRef](#)]
79. Solbrand, A.; Henningsson, A.; Södergren, S.; Lindström, H.; Hagfeldt, A.; Lindquist, S.-E. Charge Transport Properties in Dye-Sensitized Nanostructured TiO₂ Thin Film Electrodes Studied by Photoinduced Current Transients. *J. Phys. Chem. B* **1999**, *103*, 1078–1083. [[CrossRef](#)]
80. de Jongh, P.E.; Vanmaekelbergh, D. Trap-Limited Electronic Transport in Assemblies of Nanometer-Size TiO₂ Particles. *Phys. Rev. Lett.* **1996**, *77*, 3427–3430. [[CrossRef](#)] [[PubMed](#)]
81. Fisher, A.C.; Peter, L.M.; Ponomarev, E.A.; Walker, A.B.; Wijayantha, K.G.U. Intensity Dependence of the Back Reaction and Transport of Electrons in Dye-Sensitized Nanocrystalline TiO₂ Solar Cells. *J. Phys. Chem. B* **2000**, *104*, 949–958. [[CrossRef](#)]
82. Könenkamp, R. Carrier Transport in Nanoporous TiO₂ Films. *Phys. Rev. B* **2000**, *61*, 11057–11064. [[CrossRef](#)]
83. Nelson, J. Continuous-Time Random-Walk Model of Electron Transport in Nanocrystalline TiO₂ Electrodes. *Phys. Rev. B* **1999**, *59*, 15374–15380. [[CrossRef](#)]
84. Vanmaekelbergh, D.; de Jongh, P.E. Electron Transport in Disordered Semiconductors Studied by a Small Harmonic Modulation of the Steady State. *Phys. Rev. B* **2000**, *61*, 4699–4704. [[CrossRef](#)]
85. van de Lagemaat, J.; Frank, A.J. Nonthermalized Electron Transport in Dye-Sensitized Nanocrystalline TiO₂ Films: Transient Photocurrent and Random-Walk Modeling Studies. *J. Phys. Chem. B* **2001**, *105*, 11194–11205. [[CrossRef](#)]
86. Falconieri, M.; Duva, G.; Gagliardi, S. On the Response Time of Dye-Sensitized Solar Cells to Pulsed Monochromatic Illumination. *J. Phys. Appl. Phys.* **2014**, *47*, 495102. [[CrossRef](#)]
87. Bisquert, J.; Garcia-Belmonte, G.; Fabregat-Santiago, F.; Ferriols, N.S.; Bogdanoff, P.; Pereira, E.C. Doubling Exponent Models for the Analysis of Porous Film Electrodes by Impedance. Relaxation of TiO₂ Nanoporous in Aqueous Solution. *J. Phys. Chem. B* **2000**, *104*, 2287–2298. [[CrossRef](#)]
88. Shao, F.; Sun, J.; Gao, L.; Yang, S.; Luo, J. Growth of Various TiO₂ Nanostructures for Dye-Sensitized Solar Cells. *J. Phys. Chem. C* **2011**, *115*, 1819–1823. [[CrossRef](#)]
89. Bakhshayesh, A.M.; Mohammadi, M.R.; Dadar, H.; Fray, D.J. Improved efficiency of dye-sensitized solar cells aided by corn-like TiO₂ nanowires as the light scattering layer. *Electrochim. Acta* **2012**, *90*, 302–308. [[CrossRef](#)]

90. Varghese, O.K.; Paulose, M.; Grimes, C.A. Long Vertically Aligned Titania Nanotubes on Transparent Conducting Oxide for Highly Efficient Solar Cells. *Nat. Nanotechnol.* **2009**, *4*, 592–597. [[CrossRef](#)]
91. Paulose, M.; Shankar, K.; Varghese, O.K.; Mor, G.K.; Grimes, C.A. Application of Highly-Ordered TiO₂ Nanotube-Arrays in Heterojunction Dye-Sensitized Solar Cells. *J. Phys. Appl. Phys.* **2006**, *39*, 2498–2503. [[CrossRef](#)]
92. Zhong, P.; Que, W.; Zhang, J.; Jia, Q.; Wang, W.; Liao, Y.; Hu, X. Charge transport and recombination in dye-sensitized solar cells based on hybrid films of TiO₂ particles/TiO₂ nanotubes. *J. Alloys Compd.* **2011**, *509*, 7808–7813. [[CrossRef](#)]
93. Villanueva-Cab, J.; Jang, S.-R.; Halverson, A.F.; Zhu, K.; Frank, A.J. Trap-Free Transport in Ordered and Disordered TiO₂ Nanostructures. *Nano Lett.* **2014**, *14*, 2305–2309. [[CrossRef](#)]
94. Qu, J.; Li, G.R.; Gao, X.P. One-Dimensional Hierarchical Titania for Fast Reaction Kinetics of Photoanode Materials of Dye-Sensitized Solar Cells. *Energy Environ. Sci.* **2010**, *3*, 2003. [[CrossRef](#)]
95. Sauvage, F.; Di Fonzo, F.; Li Bassi, A.; Casari, C.S.; Russo, V.; Divitini, G.; Ducati, C.; Bottani, C.E.; Comte, P.; Graetzel, M. Hierarchical TiO₂ Photoanode for Dye-Sensitized Solar Cells. *Nano Lett.* **2010**, *10*, 2562–2567. [[CrossRef](#)]
96. Chen, W.; Chen, H.; Xu, G.; Xue, R.; Wang, S.; Li, Y.; Li, Y. Precise Control of Crystal Growth for Highly Efficient CsPbI₂Br Perovskite Solar Cells. *Joule* **2019**, *3*, 191–204. [[CrossRef](#)]
97. Wu, W.-Q.; Lei, B.-X.; Rao, H.-S.; Xu, Y.-F.; Wang, Y.-F.; Su, C.-Y.; Kuang, D.-B. Hydrothermal Fabrication of Hierarchically Anatase TiO₂ Nanowire Arrays on FTO Glass for Dye-Sensitized Solar Cells. *Sci. Rep.* **2013**, *3*, 1352. [[CrossRef](#)]
98. Kim, H.-S.; Lee, C.-R.; Im, J.-H.; Lee, K.-B.; Moehl, T.; Marchioro, A.; Moon, S.-J.; Humphry-Baker, R.; Yum, J.-H.; Moser, J.E.; et al. Lead Iodide Perovskite Sensitized All-Solid-State Submicron Thin Film Mesoscopic Solar Cell with Efficiency Exceeding 9%. *Sci. Rep.* **2012**, *2*, 591. [[CrossRef](#)]
99. Burschka, J.; Pellet, N.; Moon, S.-J.; Humphry-Baker, R.; Gao, P.; Nazeeruddin, M.K.; Grätzel, M. Sequential Deposition as a Route to High-Performance Perovskite-Sensitized Solar Cells. *Nature* **2013**, *499*, 316–319. [[CrossRef](#)]
100. Yadav, P.; Turren-Cruz, S.-H.; Prochowicz, D.; Tavakoli, M.M.; Pandey, K.; Zakeeruddin, S.M.; Grätzel, M.; Hagfeldt, A.; Saliba, M. Elucidation of Charge Recombination and Accumulation Mechanism in Mixed Perovskite Solar Cells. *J. Phys. Chem. C* **2018**, *122*, 15149–15154. [[CrossRef](#)]
101. Shao, J.; Yang, S.; Lei, L.; Cao, Q.; Yu, Y.; Liu, Y. Pore Size Dependent Hysteresis Elimination in Perovskite Solar Cells Based on Highly Porous TiO₂ Films with Widely Tunable Pores of 15–34 nm. *Chem. Mater.* **2016**, *28*, 7134–7144. [[CrossRef](#)]
102. Leijtens, T.; Lauber, B.; Eperon, G.E.; Stranks, S.D.; Snaith, H.J. The Importance of Perovskite Pore Filling in Organometal Mixed Halide Sensitized TiO₂-Based Solar Cells. *J. Phys. Chem. Lett.* **2014**, *5*, 1096–1102. [[CrossRef](#)]
103. Yang, Y.; Ri, K.; Mei, A.; Liu, L.; Hu, M.; Liu, T.; Li, X.; Han, H. The Size Effect of TiO₂ Nanoparticles on a Printable Mesoscopic Perovskite Solar Cell. *J. Mater. Chem. A* **2015**, *3*, 9103–9107. [[CrossRef](#)]
104. Tanaka, Y.; Lim, S.L.; Goh, W.P.; Jiang, C.; Tee, S.Y.; Ye, T.; Li, X.; Nguyen, K.H.; Lee, C.J.J.; Ding, N.; et al. Fabrication of Mesoporous Titania Nanoparticles with Controlled Porosity and Connectivity for Studying the Photovoltaic Properties in Perovskite Solar Cells. *Chem. Nano. Mat.* **2018**, *4*, 394–400. [[CrossRef](#)]
105. Sanchez, R.S.; Gonzalez-Pedro, V.; Lee, J.-W.; Park, N.-G.; Kang, Y.S.; Mora-Sero, I.; Bisquert, J. Slow Dynamic Processes in Lead Halide Perovskite Solar Cells. Characteristic Times and Hysteresis. *J. Phys. Chem. Lett.* **2014**, *5*, 2357–2363. [[CrossRef](#)]
106. Prochowicz, D.; Tavakoli, M.M.; Wolska-Pietkiewicz, M.; Jędrzejewska, M.; Trivedi, S.; Kumar, M.; Zakeeruddin, S.M.; Lewiński, J.; Graetzel, M.; Yadav, P. Suppressing Recombination in Perovskite Solar Cells via Surface Engineering of TiO₂ ETL. *Sol. Energy* **2020**, *197*, 50–57. [[CrossRef](#)]
107. Kim, H.-S.; Lee, J.-W.; Yantara, N.; Boix, P.P.; Kulkarni, S.A.; Mhaisalkar, S.; Grätzel, M.; Park, N.-G. High Efficiency Solid-State Sensitized Solar Cell-Based on Submicrometer Rutile TiO₂ Nanorod and CH₃NH₃PbI₃ Perovskite Sensitizer. *Nano Lett.* **2013**, *13*, 2412–2417. [[CrossRef](#)] [[PubMed](#)]
108. Gao, X.; Li, J.; Baker, J.; Hou, Y.; Guan, D.; Chen, J.; Yuan, C. Enhanced Photovoltaic Performance of Perovskite CH₃NH₃PbI₃ Solar Cells with Freestanding TiO₂ Nanotube Array Films. *Chem. Commun.* **2014**, *50*, 6368–6371. [[CrossRef](#)] [[PubMed](#)]
109. Salazar, R.; Altomare, M.; Lee, K.; Tripathy, J.; Kirchgeorg, R.; Nguyen, N.T.; Mokhtar, M.; Alshehri, A.; Al-Thabaiti, S.A.; Schmuki, P. Use of Anodic TiO₂ Nanotube Layers as Mesoporous Scaffolds for Fabricating CH₃NH₃PbI₃ Perovskite-Based Solid-State Solar Cells. *Chem. Electro. Chem.* **2015**, *2*, 824–828. [[CrossRef](#)]
110. Lan, Z.; Xu, X.; Zhang, X.; Tang, J.; Zhang, L.; He, X.; Wu, J. Low-Temperature Solution-Processed Efficient Electron-Transporting Layers Based on BF₄⁻-Capped TiO₂ Nanorods for High-Performance Planar Perovskite Solar Cells. *J. Mater. Chem. C* **2018**, *6*, 334–341. [[CrossRef](#)]
111. Wu, S.; Chen, C.; Wang, J.; Xiao, J.; Peng, T. Controllable Preparation of Rutile TiO₂ Nanorod Array for Enhanced Photovoltaic Performance of Perovskite Solar Cells. *ACS Appl. Energy Mater.* **2018**, *1*, 1649–1657. [[CrossRef](#)]
112. Dharani, S.; Mulmudi, H.K.; Yantara, N.; Trang, P.T.T.; Park, N.G.; Graetzel, M.; Mhaisalkar, S.; Mathews, N.; Boix, P.P. High Efficiency Electrospun TiO₂ Nanofiber Based Hybrid Organic–Inorganic Perovskite Solar Cell. *Nanoscale* **2014**, *6*, 1675–1679. [[CrossRef](#)] [[PubMed](#)]
113. Tao, H.; Ke, W.; Wang, J.; Liu, Q.; Wan, J.; Yang, G.; Fang, G. Perovskite solar cell based on network nanoporous layer consisted of TiO₂ nanowires and its interface optimization. *J. Power Source* **2015**, *290*, 144–152. [[CrossRef](#)]
114. Mahmood, K.; Swain, B.S.; Amassian, A. Core–Shell Heterostructured Metal Oxide Arrays Enable Superior Light-Harvesting and Hysteresis-Free Mesoscopic Perovskite Solar Cells. *Nanoscale* **2015**, *7*, 12812–12819. [[CrossRef](#)] [[PubMed](#)]

115. Wu, W.-Q.; Wang, L. 3D Branched Nanowire-Coated Macroporous Titania Thin Films for Efficient Perovskite Solar Cells. *Adv. Funct. Mater.* **2018**, *28*, 1804356. [[CrossRef](#)]
116. Wu, W.-Q.; Xu, Y.-F.; Liao, J.-F.; Wang, L.; Kuang, D.-B. Branched Titania Nanostructures for Efficient Energy Conversion and Storage: A Review on Design Strategies, Structural Merits and Multifunctionalities. *Nano Energy* **2019**, *62*, 791–809. [[CrossRef](#)]
117. Brown, T.M.; De Rossi, F.; Di Giacomo, F.; Mincuzzi, G.; Zardetto, V.; Reale, A.; Di Carlo, A. Progress in flexible dye solar cell materials, processes and devices. *J. Mater. Chem. A* **2014**, *2*, 10788–10817. [[CrossRef](#)]
118. Li, G.; Sheng, L.; Li, T.; Hu, J.; Li, P.; Wang, K. Engineering flexible dye-sensitized solar cells for portable electronics. *Solar Energy* **2019**, *177*, 80–98. [[CrossRef](#)]
119. Cao, Y.; Liu, Y.; Zakeeruddin, S.M.; Hagfeldt, A.; Grätzel, M. Direct contact of selective charge extraction layers enables high-efficiency molecular photovoltaics. *Joule* **2018**, *2*, 1108–1117. [[CrossRef](#)]
120. Wang, B.; Shen, S.; Mao, S.S. Black TiO₂ for Solar Hydrogen Conversion. *J. Materiomics* **2017**, *3*, 96–111. [[CrossRef](#)]
121. Jafari, T.; Moharreri, E.; Amin, A.S.; Miao, R.; Song, W.; Suib, S.L. Photocatalytic Water Splitting-The Untamed Dream: A Review of Recent Advances. *Molecules* **2016**, *21*, E900. [[CrossRef](#)] [[PubMed](#)]
122. Ni, M.; Leung, M.K.H.; Leung, D.Y.C.; Sumathy, K. A Review and Recent Developments in Photocatalytic Water-Splitting Using TiO₂ for Hydrogen Production. *Renew. Sustain. Energy Rev.* **2007**, *11*, 401–425. [[CrossRef](#)]
123. Khan, S.U.M.; Al-Shahry, M.; Ingler, W.B. Efficient Photochemical Water Splitting by a Chemically Modified N-TiO₂. *Science* **2002**, *297*, 2243–2245. [[CrossRef](#)]
124. Kasani, S.; Curtin, K.; Wu, N. A Review of 2D and 3D Plasmonic Nanostructure Array Patterns: Fabrication, Light Management and Sensing Applications. *Nanophotonics* **2019**, *8*, 2065–2089. [[CrossRef](#)]
125. Wang, L.; Wang, Y.; Schmuki, P.; Kment, S.; Zboril, R. Nanostar Morphology of Plasmonic Particles Strongly Enhances Photoelectrochemical Water Splitting of TiO₂ Nanorods with Superior Incident Photon-to-Current Conversion Efficiency in Visible/near-Infrared Region. *Electrochim. Acta* **2018**, *260*, 212–220. [[CrossRef](#)]
126. Sun, X.; Liu, H.; Dong, J.; Wei, J.; Zhang, Y. Preparation and Characterization of Ce/N-Co doped TiO₂ Particles for Production of H₂ by Photocatalytic Splitting Water Under Visible Light. *Catal. Lett.* **2010**, *135*, 219–225. [[CrossRef](#)]
127. Youngblood, W.J.; Lee, S.-H.A.; Maeda, K.; Mallouk, T.E. Visible Light Water Splitting Using Dye-Sensitized Oxide Semiconductors. *Acc. Chem. Res.* **2009**, *42*, 1966–1973. [[CrossRef](#)]
128. Kment, S.; Riboni, F.; Pausova, S.; Wang, L.; Wang, L.; Han, H.; Hubicka, Z.; Krysa, J.; Schmuki, P.; Zboril, R. Photoanodes Based on TiO₂ and α -Fe₂O₃ for Solar Water Splitting-Superior Role of 1D Nanoarchitectures and of Combined Heterostructures. *Chem. Soc. Rev.* **2017**, *46*, 3716–3769. [[CrossRef](#)] [[PubMed](#)]
129. Bard, A.J.; Bocarsly, A.B.; Fan, F.R.F.; Walton, E.G.; Wrighton, M.S. The Concept of Fermi Level Pinning at Semiconductor/Liquid Junctions. Consequences for Energy Conversion Efficiency and Selection of Useful Solution Redox Couples in Solar Devices. *J. Am. Chem. Soc.* **1980**, *102*, 3671–3677. [[CrossRef](#)]
130. Fujishima, A.; Honda, K. Electrochemical Photolysis of Water at a Semiconductor Electrode. *Nature* **1972**, *238*, 37–38. [[CrossRef](#)] [[PubMed](#)]
131. Eftekhari, A.; Babu, V.J.; Ramakrishna, S. Photoelectrode nanomaterials for photoelectrochemical water splitting. *Int. J. Hydrogen Energy* **2017**, *42*, 11078–11109. [[CrossRef](#)]
132. Kapilashrami, M.; Zhang, Y.; Liu, Y.S.; Hagfeldt, A.; Guo, J. Probing the optical property and electronic structure of TiO₂ nanomaterials for renewable energy applications. *Chem. Rev.* **2014**, *114*, 9662–9707. [[CrossRef](#)]
133. Jiang, C.; Moniz, S.J.; Wang, A.; Zhang, T.; Tang, J. Photoelectrochemical devices for solar water splitting—materials and challenges. *Chem. Soc. Rev.* **2017**, *46*, 4645–4660. [[CrossRef](#)]
134. Chen, Z.; Jaramillo, T.F.; Deutsch, T.G.; Kleiman-Shwarsstein, A.; Forman, A.J.; Gaillard, N.; Garland, R.; Takanabe, K.; Heske, C.; Sunkara, M.; et al. Accelerating Materials Development for Photoelectrochemical Hydrogen Production: Standards for Methods, Definitions, and Reporting Protocols. *J. Mater. Res.* **2010**, *25*, 3–16. [[CrossRef](#)]
135. Ibadurrohman, M.; Hellgardt, K. Morphological Modification of TiO₂ Thin Films as Highly Efficient Photoanodes for Photoelectrochemical Water Splitting. *ACS Appl. Mater. Interfaces* **2015**, *7*, 9088–9097. [[CrossRef](#)]
136. Chen, Z.; Deutsch, T.G.; Dinh, H.N.; Domen, K.; Emery, K.; Forman, A.J.; Gaillard, N.; Garland, R.; Heske, C.; Jaramillo, T.F.; et al. Efficiency Definitions in the Field of PEC. In *Photoelectrochemical Water Splitting: Standards, Experimental Methods, and Protocols*; Springer Briefs in Energy; Chen, Z., Dinh, H.N., Miller, E., Eds.; Springer: New York, NY, USA, 2013; pp. 7–16. [[CrossRef](#)]
137. Cai, J.; Shen, J.; Zhang, X.; Ng, Y.H.; Huang, J.; Guo, W.; Lin, C.; Lai, Y. Light-Driven Sustainable Hydrogen Production Utilizing TiO₂ Nanostructures: A Review. *Small Methods* **2019**, *3*, 1800184. [[CrossRef](#)]
138. Hwang, Y.J.; Boukai, A.; Yang, P. High Density N-Si/n-TiO₂ Core/Shell Nanowire Arrays with Enhanced Photoactivity. *Nano Lett.* **2009**, *9*, 410–415. [[CrossRef](#)] [[PubMed](#)]
139. Gupta, N.M. Factors Affecting the Efficiency of a Water Splitting Photocatalyst: A Perspective. *Renew. Sustain. Energy Rev.* **2017**, *71*, 585–601. [[CrossRef](#)]
140. Osterloh, F.E. Inorganic Nanostructures for Photoelectrochemical and Photocatalytic Water Splitting. *Chem. Soc. Rev.* **2013**, *42*, 2294–2320. [[CrossRef](#)]
141. Leng, W.H.; Barnes, P.R.F.; Juozapavicius, M.; O'Regan, B.C.; Durrant, J.R. Electron Diffusion Length in Mesoporous Nanocrystalline TiO₂ Photoelectrodes during Water Oxidation. *J. Phys. Chem. Lett.* **2010**, *1*, 967–972. [[CrossRef](#)]

142. Qiu, Y.; Leung, S.-F.; Wei, Z.; Lin, Q.; Zheng, X.; Zhang, Y.; Fan, Z.; Yang, S. Enhanced Charge Collection for Splitting of Water Enabled by an Engineered Three-Dimensional Nanospire Array. *J. Phys. Chem. C* **2014**, *118*, 22465–22472. [[CrossRef](#)]
143. Yu, Z.; Liu, H.; Zhu, M.; Li, Y.; Li, W. Interfacial Charge Transport in 1D TiO₂ Based Photoelectrodes for Photoelectrochemical Water Splitting. *Small* **2021**, *17*, 1903378. [[CrossRef](#)]
144. Shankar, K.; Basham, J.I.; Allam, N.K.; Varghese, O.K.; Mor, G.K.; Feng, X.; Paulose, M.; Seabold, J.A.; Choi, K.-S.; Grimes, C.A. Recent Advances In the Use of TiO₂ Nanotube and Nanowire Arrays for Oxidative Photoelectrochemistry. *J. Phys. Chem. C* **2009**, *113*, 6327–6359. [[CrossRef](#)]
145. Ozkan, S.; Nguyen, N.T.; Mazare, A.; Schmuki, P. Optimized Spacing between TiO₂ Nanotubes for Enhanced Light Harvesting and Charge Transfer. *Chem. Electro. Chem.* **2018**, *5*, 3183–3190. [[CrossRef](#)]
146. Chiarello, G.L.; Zuliani, A.; Ceresoli, D.; Martinazzo, R.; Selli, E. Exploiting the Photonic Crystal Properties of TiO₂ Nanotube Arrays To Enhance Photocatalytic Hydrogen Production. *ACS Catal.* **2016**, *6*, 1345–1353. [[CrossRef](#)]
147. Escudero, J.C.; Cervera-March, S.; Giménez, J.; Simarro, R. Preparation and Characterization of Pt(RuO₂)/TiO₂ Catalysts: Test in a Continuous Water Photolysis System. *J. Catal.* **1990**, *123*, 319–332. [[CrossRef](#)]
148. Hartig, K.J.; Getoff, N.; Rumpelmayer, G.; Popkirov, G.; Kotchev, K.; Kanev, S.; Veziroğlu, T.N.; Getoff, N.; Weinzierl, P. (Eds.) *Hydrogen Energy Progress VI*; Pergamon Press: Oxford, UK, 1986; Volume 2, p. 546.
149. Berardo, E.; Zwijnenburg, M.A. Modeling the Water Splitting Activity of a TiO₂ Rutile Nanoparticle. *J. Phys. Chem. C* **2015**, *119*, 13384–13393. [[CrossRef](#)]
150. Banno, H.; Kariya, B.; Izu, N.; Ogawa, M.; Miwa, S.; Sawada, K.; Tsuge, J.; Imaizumi, S.; Kato, H.; Tokutake, K.; et al. Effect of TiO₂ Crystallite Diameter on Photocatalytic Water Splitting Rate. *Green Sustain. Chem.* **2014**, *4*, 87–94. [[CrossRef](#)]
151. Hidalgo, D.; Messina, R.; Sacco, A.; Manfredi, D.; Vankova, S.; Garrone, E.; Saracco, G.; Hernández, S. Thick Mesoporous TiO₂ Films through a Sol–Gel Method Involving a Non-Ionic Surfactant: Characterization and Enhanced Performance for Water Photo-Electrolysis. *Int. J. Hydrogen Energy* **2014**, *39*, 21512–21522. [[CrossRef](#)]
152. Modesto-Lopez, L.B.; Biswas, P. Role of the Effective Electrical Conductivity of Nanosuspensions in the Generation of TiO₂ Agglomerates with Electrospray. *J. Aerosol Sci.* **2010**, *41*, 790–804. [[CrossRef](#)]
153. Hartmann, P.; Lee, D.-K.; Smarsly, B.M.; Janek, J. Mesoporous TiO₂: Comparison of Classical Sol–Gel and Nanoparticle Based Photoelectrodes for the Water Splitting Reaction. *ACS Nano* **2010**, *4*, 3147–3154. [[CrossRef](#)]
154. Paulose, M.; Varghese, O.K.; Shankar, K.; Mor, G.K.; Grimes, C.A. Photoelectrochemical Properties of Highly-Ordered Titania Nanotube-Arrays. *MRS Online Proc. Libr. (OPL)* **2004**, *837*, N3.13. [[CrossRef](#)]
155. Fujimoto, M.; Kado, T.; Takashima, W.; Kaneto, K.; Hayase, S. Dye-Sensitized Solar Cells Fabricated by Electrospray Coating Using TiO₂ Nanocrystal Dispersion Solution. *J. Electrochem. Soc.* **2006**, *153*, A826. [[CrossRef](#)]
156. Liu, M.; de Leon Snapp, N.; Park, H. Water Photolysis with a Cross-Linked Titanium Dioxide Nanowire Anode. *Chem. Sci.* **2011**, *2*, 80–87. [[CrossRef](#)]
157. Zhang, Z.; Wang, P. Optimization of Photoelectrochemical Water Splitting Performance on Hierarchical TiO₂ Nanotube Arrays. *Energy Environ. Sci.* **2012**, *5*, 6506. [[CrossRef](#)]
158. Nozik, A.J.; Miller, J. Introduction to Solar Photon Conversion. *Chem. Rev.* **2010**, *110*, 6443–6445. [[CrossRef](#)]
159. Eidsvåg, H.; Bentouba, S.; Vajeeston, P.; Yohi, S.; Velauthapillai, D. TiO₂ as a Photocatalyst for Water Splitting—An Experimental and Theoretical Review. *Molecules* **2021**, *26*, 1687. [[CrossRef](#)]
160. Thimsen, E.; Rastgar, N.; Biswas, P. Nanostructured TiO₂ Films with Controlled Morphology Synthesized in a Single Step Process: Performance of Dye-Sensitized Solar Cells and Photo Water Splitting. *J. Phys. Chem. C* **2008**, *112*, 4134–4140. [[CrossRef](#)]
161. Regonini, D.; Clemens, F.J. Anodized TiO₂ Nanotubes: Effect of Anodizing Time on Film Length, Morphology and Photoelectrochemical Properties. *Mater. Lett.* **2015**, *142*, 97–101. [[CrossRef](#)]
162. Palmas, S.; Polcaro, A.M.; Ruiz, J.R.; Da Pozzo, A.; Mascia, M.; Vacca, A. TiO₂ Photoanodes for Electrically Enhanced Water Splitting. *Int. J. Hydrogen Energy* **2010**, *35*, 6561–6570. [[CrossRef](#)]
163. Mor, G.K.; Varghese, O.K.; Paulose, M.; Shankar, K.; Grimes, C.A. A Review on Highly Ordered, Vertically Oriented TiO₂ Nanotube Arrays: Fabrication, Material Properties, and Solar Energy Applications. *Sol. Energy Mater. Sol. Cells* **2006**, *90*, 2011–2075. [[CrossRef](#)]
164. Wang, D.; Zhang, X.; Sun, P.; Lu, S.; Wang, L.; Wang, C.; Liu, Y. Photoelectrochemical Water Splitting with Rutile TiO₂ Nanowires Array: Synergistic Effect of Hydrogen Treatment and Surface Modification with Anatase Nanoparticles. *Electrochim. Acta* **2014**, *130*, 290–295. [[CrossRef](#)]
165. Hwang, Y.J.; Hahn, C.; Liu, B.; Yang, P. Photoelectrochemical Properties of TiO₂ Nanowire Arrays: A Study of the Dependence on Length and Atomic Layer Deposition Coating. *ACS Nano* **2012**, *6*, 5060–5069. [[CrossRef](#)]
166. Mao, Y.; Ning, C.; Zhang, N.; Hu, Y.; Li, M.; Yang, H.; Chen, S.; Su, S.; Liang, E. Enhancing Photoelectrochemical Performance of TiO₂ Nanowires through a Facile Acid Treatment Method. *J. Electrochem. Soc.* **2018**, *165*, H799. [[CrossRef](#)]
167. Mali, M.G.; An, S.; Liou, M.; Al-Deyab, S.S.; Yoon, S.S. Photoelectrochemical solar water splitting using electrospun TiO₂ nanofibers. *Appl. Surf. Sci.* **2015**, *328*, 109–114. [[CrossRef](#)]
168. Li, W.; Bai, Y.; Zhuang, W.; Chan, K.-Y.; Liu, C.; Yang, Z.; Feng, X.; Lu, X. Highly Crystalline Mesoporous TiO₂(B) Nanofibers. *J. Phys. Chem. C* **2014**, *118*, 3049–3055. [[CrossRef](#)]
169. Ongaro, M.; Mardegan, A.; Stortini, A.M.; Signoretto, M.; Ugo, P. Arrays of Templated TiO₂ Nanofibres as Improved Photoanodes for Water Splitting under Visible Light. *Nanotechnology* **2015**, *26*, 165402. [[CrossRef](#)] [[PubMed](#)]

170. Wolcott, A.; Smith, W.A.; Kuykendall, T.R.; Zhao, Y.; Zhang, J.Z. Photoelectrochemical Water Splitting Using Dense and Aligned TiO₂ Nanorod Arrays. *Small* **2009**, *5*, 104–111. [[CrossRef](#)] [[PubMed](#)]
171. Fàbrega, C.; Andreu, T.; Tarancón, A.; Flox, C.; Morata, A.; Calvo-Barrio, L.; Morante, J.R. Optimization of Surface Charge Transfer Processes on Rutile TiO₂ Nanorods Photoanodes for Water Splitting. *Int. J. Hydrogen Energy* **2013**, *38*, 2979–2985. [[CrossRef](#)]
172. Paulose, M.; Shankar, K.; Yoriya, S.; Prakasam, H.E.; Varghese, O.K.; Mor, G.K.; Latempa, T.A.; Fitzgerald, A.; Grimes, C.A. Anodic Growth of Highly Ordered TiO₂ Nanotube Arrays to 134 mm in Length. *J. Phys. Chem. B* **2006**, *110*, 16179–16184. [[CrossRef](#)]
173. Mor, G.K.; Shankar, K.; Paulose, M.; Varghese, O.K.; Grimes, C.A. Enhanced Photocleavage of Water Using Titania Nanotube Arrays. *Nano Lett.* **2005**, *5*, 191–195. [[CrossRef](#)]
174. Liang, S.; He, J.; Sun, Z.; Liu, Q.; Jiang, Y.; Cheng, H.; He, B.; Xie, Z.; Wei, S. Improving Photoelectrochemical Water Splitting Activity of TiO₂ Nanotube Arrays by Tuning Geometrical Parameters. *J. Phys. Chem. C* **2012**, *116*, 9049–9053. [[CrossRef](#)]
175. Ennaceri, H.; Fischer, K.; Hanus, K.; Chemseddine, A.; Prager, A.; Griebel, J.; Kühnert, M.; Schulze, A.; Abel, B. Effect of Morphology on the Photoelectrochemical Activity of TiO₂ Self-Organized Nanotube Arrays. *Catalysts* **2020**, *10*, 279. [[CrossRef](#)]
176. Mohamed, A.M.; Aljaber, A.S.; AlQaradawi, S.Y.; Allam, N.K. TiO₂ Nanotubes with Ultrathin Walls for Enhanced Water Splitting. *Chem. Commun.* **2015**, *51*, 12617–12620. [[CrossRef](#)]
177. Kim, H.S.; Ahn, K.-S.; Kang, S.H. Enhancing Photoelectrochemical Water Splitting Performance of TiO₂ nanotube Arrays by Controlling Morphological Properties. *Electron. Mater. Lett.* **2014**, *10*, 345–349. [[CrossRef](#)]
178. Xu, X.; Fang, X.; Zhai, T.; Zeng, H.; Liu, B.; Hu, X.; Bando, Y.; Golberg, D. Tube-in-Tube TiO₂ Nanotubes with Porous Walls: Fabrication, Formation Mechanism, and Photocatalytic Properties. *Small* **2011**, *7*, 445–449. [[CrossRef](#)] [[PubMed](#)]
179. Adán, C.; Marugán, J.; Sánchez, E.; Pablos, C.; Van Grieken, R. Understanding the effect of morphology on the photocatalytic activity of TiO₂ nanotube array electrodes. *Electrochim. Acta* **2016**, *191*, 521–529. [[CrossRef](#)]
180. Nishanthi, S.T.; Subramanian, E.; Sundarakannan, B.; Pathinettam Padiyan, D. An insight into the influence of morphology on the photoelectrochemical activity of TiO₂ nanotube arrays. *Sol. Energy Mater. Sol. Cells* **2015**, *132*, 204–209. [[CrossRef](#)]
181. Varghese, O.K.; Paulose, M.; Shankar, K.; Mor, G.K.; Grimes, C.A. Water-Photolysis Properties of Micron-Length Highly-Ordered Titania Nanotube-Arrays. *J. Nanosci. Nanotechnol.* **2005**, *5*, 1158–1165. [[CrossRef](#)] [[PubMed](#)]
182. Shankar, K.; Mor, G.K.; Prakasam, H.E.; Yoriya, S.; Paulose, M.; Varghese, O.K.; Grimes, C.A. Highly-Ordered TiO₂ Nanotube Arrays up to 220 Mm in Length: Use in Water photoelectrolysis and Dye-Sensitized Solar Cells. *Nanotechnology* **2007**, *18*, 065707. [[CrossRef](#)]
183. Kusior, A.; Wnuk, A.; Trenczek-Zajac, A.; Zakrzewska, K.; Radecka, M. TiO₂ nanostructures for photoelectrochemical cells (PECs). *Int. J. Hydrogen Energy* **2015**, *40*, 4936–4944. [[CrossRef](#)]
184. Butburee, T.; Bai, Y.; Wang, H.; Chen, H.; Wang, Z.; Liu, G.; Zou, J.; Khemthong, P.; Lu, G.Q.M.; Wang, L. 2D Porous TiO₂ Single-Crystalline Nanostructure Demonstrating High Photo-Electrochemical Water Splitting Performance. *Adv. Mater.* **2018**, *30*, 1705666. [[CrossRef](#)] [[PubMed](#)]
185. Cho, I.S.; Chen, Z.; Forman, A.J.; Kim, D.R.; Rao, P.M.; Jaramillo, T.F.; Zheng, X. Branched TiO₂ Nanorods for Photoelectrochemical Hydrogen Production. *Nano Lett.* **2011**, *11*, 4978–4984. [[CrossRef](#)]
186. Zhang, R.; Shen, D.; Xu, M.; Feng, D.; Li, W.; Zheng, G.; Che, R.; Elzatahry, A.A.; Zhao, D. Ordered Macro-/Mesoporous Anatase Films with High Thermal Stability and Crystallinity for Photoelectrocatalytic Water-Splitting. *Adv. Energy Mater.* **2014**, *4*, 1301725. [[CrossRef](#)]
187. Yang, J.S.; Liao, W.P.; Wu, J.J. Morphology and interfacial energetics controls for hierarchical anatase/rutile TiO₂ nanostructured array for efficient photoelectrochemical water splitting. *ACS Appl. Mater. Interfaces* **2013**, *5*, 7425–7431. [[CrossRef](#)] [[PubMed](#)]
188. Ali, H.M.; Sajid, M.U.; Arshad, A. Heat transfer applications of TiO₂ nanofluids. In *Application of Titanium dioxide*; Janus, M., Ed.; IntechOpen: London, UK, 2017; pp. 181–200. [[CrossRef](#)]
189. Tawfik, M.M. Experimental Studies of Nanofluid Thermal Conductivity Enhancement and Applications: A Review. *Renew. Sustain. Energy Rev.* **2017**, *75*, 1239–1253. [[CrossRef](#)]
190. Qiu, L.; Zhu, N.; Feng, Y.; Michaelides, E.E.; Żyła, G.; Jing, D.; Zhang, X.; Norris, P.M.; Markides, C.N.; Mahian, O. A Review of Recent Advances in Thermophysical Properties at the Nanoscale: From Solid State to Colloids. *Phys. Rep.* **2020**, *843*, 1–81. [[CrossRef](#)]
191. Iqbal, S.M.; Arulprakasajothi, M.; Raja, N.D.; Bosko, S.M.J.; Teja, M.B. Investigation On The Thermal Behaviour Of Titanium Dioxide Nanofluid. *Mater. Today Proc.* **2018**, *5*, 20608–20613. [[CrossRef](#)]
192. Gonçalves, I.; Souza, R.; Coutinho, G.; Miranda, J.; Moita, A.; Pereira, J.E.; Moreira, A.; Lima, R. Thermal Conductivity of Nanofluids: A Review on Prediction Models, Controversies and Challenges. *Appl. Sci.* **2021**, *11*, 2525. [[CrossRef](#)]
193. Murshed, S.M.S.; Leong, K.C.; Yang, C. Investigations of Thermal Conductivity and Viscosity of Nanofluids. *Int. J. Therm. Sci.* **2008**, *47*, 560–568. [[CrossRef](#)]
194. Yang, L.; Hu, Y. Toward TiO₂ Nanofluids—Part 2: Applications and Challenges. *Nanoscale Res. Lett.* **2017**, *12*, 446. [[CrossRef](#)] [[PubMed](#)]
195. Okonkwo, E.C.; Wole-Osho, I.; Almanassra, I.W.; Abdullatif, Y.M.; Al-Ansari, T. An Updated Review of Nanofluids in Various Heat Transfer Devices. *J. Therm. Anal. Calorim.* **2021**, *145*, 2817–2872. [[CrossRef](#)]
196. Elsaid, K.; Olabi, A.G.; Wilberforce, T.; Abdelkareem, M.A.; Sayed, E.T. Environmental Impacts of Nanofluids: A Review. *Sci. Total Environ.* **2021**, *763*, 144202. [[CrossRef](#)] [[PubMed](#)]
197. Maxwell, J.C. A Treatise on Electricity and Magnetism. *Nature* **1873**, *7*, 478–480. [[CrossRef](#)]

198. Bruggeman, D.A.G. Berechnung verschiedener physikalischer Konstanten von heterogenen Substanzen. I. Dielektrizitätskonstanten und Leitfähigkeiten der Mischkörper aus isotropen Substanzen. *Ann. Der Phys.* **1935**, *416*, 636–664. [[CrossRef](#)]
199. Stroud, D. The Effective Medium Approximations: Some Recent Developments. *Superlattices Microstruct.* **1998**, *23*, 567–573. [[CrossRef](#)]
200. Garnett, J.M. Colours in metal glasses and in metallic films. In *Philosophical Transactions of the Royal Society of London; Series A; Containing Papers of a Mathematical or Physical Character*; Royal Society: London, UK, 1904; Volume 203, pp. 385–420. [[CrossRef](#)]
201. Hamilton, R.L.; Crosser, O.K. Thermal Conductivity of Heterogeneous Two-Component Systems. *Ind. Eng. Chem. Fundam.* **1962**, *1*, 187–191. [[CrossRef](#)]
202. Hasselman, D.P.H.; Lloyd, F.J. Effective Thermal Conductivity of Composites with Interfacial Thermal Barrier Resistance. *J. Compos. Mater.* **1987**, *21*, 508–515. [[CrossRef](#)]
203. Yu, W.; Choi, S.U.S. The Role of Interfacial Layers in the Enhanced Thermal Conductivity of Nanofluids: A Renovated Maxwell Model. *J. Nanopart. Res.* **2003**, *5*, 167–171. [[CrossRef](#)]
204. Nan, C.-W.; Birringer, R.; Clarke, D.R.; Gleiter, H. Effective Thermal Conductivity of Particulate Composites with Interfacial Thermal Resistance. *J. Appl. Phys.* **1997**, *81*, 6692–6699. [[CrossRef](#)]
205. Wilson, O.M.; Hu, X.; Cahill, D.G.; Braun, P.V. Colloidal Metal Particles as Probes of Nanoscale Thermal Transport in Fluids. *Phys. Rev. B* **2002**, *66*, 224301. [[CrossRef](#)]
206. Huxtable, S.T.; Cahill, D.G.; Shenogin, S.; Xue, L.; Ozisik, R.; Barone, P.; Usrey, M.; Strano, M.S.; Siddons, G.; Shim, M.; et al. Interfacial Heat Flow in Carbon Nanotube Suspensions. *Nat. Mater.* **2003**, *2*, 731–734. [[CrossRef](#)]
207. Pil Jang, S.; Choi, S.U.S. Effects of Various Parameters on Nanofluid Thermal Conductivity. *J. Heat Transf.* **2006**, *129*, 617–623. [[CrossRef](#)]
208. Jang, S.P.; Choi, S.U.S. Role of Brownian Motion in the Enhanced Thermal Conductivity of Nanofluids. *Appl. Phys. Lett.* **2004**, *84*, 4316–4318. [[CrossRef](#)]
209. Koo, J.; Kleinstreuer, C. A new thermal conductivity model for nanofluids. *J. Nanopart. Res.* **2004**, *6*, 577–588. [[CrossRef](#)]
210. Shukla, R.K.; Dhir, V.K. Numerical Study of the Effective Thermal Conductivity of Nanofluids. In *American Society of Mechanical Engineers Digital Collection*; American Society of Mechanical Engineers: New York, NY, USA, 2009; pp. 449–457. [[CrossRef](#)]
211. Shukla, R.K.; Dhir, V.K. Effect of Brownian Motion on Thermal Conductivity of Nanofluids. *J. Heat Transf.* **2008**, *130*, 042406. [[CrossRef](#)]
212. Kumar, D.H.; Patel, H.E.; Kumar, V.R.R.; Sundararajan, T.; Pradeep, T.; Das, S.K. Model for Heat Conduction in Nanofluids. *Phys. Rev. Lett.* **2004**, *93*, 144301. [[CrossRef](#)] [[PubMed](#)]
213. Prasher, R.; Bhattacharya, P.; Phelan, P.E. Brownian-Motion-Based Convective-Conductive Model for the Effective Thermal Conductivity of Nanofluids. *J. Heat Transf.* **2005**, *128*, 588–595. [[CrossRef](#)]
214. Evans, W.; Fish, J.; Keblinski, P. Role of Brownian Motion Hydrodynamics on Nanofluid Thermal Conductivity. *Appl. Phys. Lett.* **2006**, *88*, 093116. [[CrossRef](#)]
215. Keblinski, P.; Eastman, J.A.; Cahill, D.G. Nanofluids for Thermal Transport. *Mater. Today* **2005**, *8*, 36–44. [[CrossRef](#)]
216. Bhattacharya, P.; Saha, S.K.; Yadav, A.; Phelan, P.E.; Prasher, R.S. Brownian Dynamics Simulation to Determine the Effective Thermal Conductivity of Nanofluids. *J. Appl. Phys.* **2004**, *95*, 6492–6494. [[CrossRef](#)]
217. Wang, Z.L.; Tang, D.W.; Liu, S.; Zheng, X.H.; Araki, N. Thermal-Conductivity and Thermal-Diffusivity Measurements of Nanofluids by 3 ω Method and Mechanism Analysis of Heat Transport. *Int. J. Thermophys.* **2007**, *28*, 1255–1268. [[CrossRef](#)]
218. Zhang, X.; Gu, H.; Fujii, M. Effective Thermal Conductivity and Thermal Diffusivity of Nanofluids Containing Spherical and Cylindrical Nanoparticles. *Exp. Therm. Fluid Sci.* **2007**, *31*, 593–599. [[CrossRef](#)]
219. Turgut, A.; Tavman, I.; Chirtoc, M.; Schuchmann, H.P.; Sauter, C.; Tavman, S. Thermal Conductivity and Viscosity Measurements of Water-Based TiO₂ Nanofluids. *Int. J. Thermophys.* **2009**, *30*, 1213–1226. [[CrossRef](#)]
220. Rondino, F.; D’Amato, R.; Terranova, G.; Borsella, E.; Falconieri, M. Thermal Diffusivity Enhancement in Nanofluids Based on Pyrolytic Titania Nanopowders: Importance of Aggregate Morphology. *J. Raman Spectrosc.* **2014**, *45*, 528–532. [[CrossRef](#)]
221. Hamid, K.A.; Azmi, W.; Mamat, R.; Usri, N. Thermal Conductivity Enhancement of TiO₂ Nanofluid in Water and Ethylene Glycol (EG) Mixture. *Indian J. Pure Appl. Phys.* **2016**, *54*, 651–655.
222. Ali, H.M.; Babar, H.; Shah, T.R.; Sajid, M.U.; Qasim, M.A.; Javed, S. Preparation Techniques of TiO₂ Nanofluids and Challenges: A Review. *Appl. Sci.* **2018**, *8*, 587. [[CrossRef](#)]
223. Coccia, G.; Tomassetti, S.; Di Nicola, G. Thermal Conductivity of Nanofluids: A Review of the Existing Correlations and a Scaled Semi-Empirical Equation. *Renew. Sustain. Energy Rev.* **2021**, *151*, 111573. [[CrossRef](#)]
224. Zagabathuni, A.; Ghosh, S.; Pabi, S.K. The Difference in the Thermal Conductivity of Nanofluids Measured by Different Methods and Its Rationalization. *Beilstein J. Nanotechnol.* **2016**, *7*, 2037–2044. [[CrossRef](#)] [[PubMed](#)]
225. Zhao, D.; Qian, X.; Gu, X.; Jajja, S.; Yang, R. Measurement Techniques for Thermal Conductivity and Interfacial Thermal Conductance of Bulk and Thin Film Materials. *J. Electron. Packag.* **2016**, *138*, 040802. [[CrossRef](#)]
226. Roetzel, W.; Prinzen, S.; Wandelt, M. Temperature Oscillation Technique for Determination of Local Convective Heat Transfer Coefficients without Fluid Temperature Measurement. *Chem. Eng. Technol.* **1993**, *16*, 89–93. [[CrossRef](#)]
227. Gustafsson, S.E.; Karawacki, E.; Khan, M.N. Transient Hot-Strip Method for Simultaneously Measuring Thermal Conductivity and Thermal Diffusivity of Solids and Fluids. *J. Phys. Appl. Phys.* **1979**, *12*, 1411–1421. [[CrossRef](#)]

228. Eichler, H.J.; Günter, P.; Pohl, D.W. (Eds.) Mechanisms of Grating Formation and Grating Materials. In *Laser-Induced Dynamic Gratings*; Springer Series in Optical Sciences; Springer: Berlin/Heidelberg, Germany, 1986; pp. 38–93. [[CrossRef](#)]
229. Venerus, D.C.; Schieber, J.D.; Iddir, H.; Guzman, J.D.; Broerman, A.W. Measurement of Thermal Diffusivity in Polymer Melts Using Forced Rayleigh Light Scattering. *J. Polym. Sci. Part B Polym. Phys.* **1999**, *37*, 1069–1078. [[CrossRef](#)]
230. Wang, B.-X.; Zhou, L.-P.; Peng, X.-F. A Fractal Model for Predicting the Effective Thermal Conductivity of Liquid with Suspension of Nanoparticles. *Int. J. Heat Mass Transf.* **2003**, *46*, 2665–2672. [[CrossRef](#)]
231. Prasher, R.; Evans, W.; Meakin, P.; Fish, J.; Phelan, P.; Keblinski, P. Effect of aggregation on thermal conduction in colloidal nanofluids. *Appl. Phys. Lett.* **2006**, *89*, 143119. [[CrossRef](#)]
232. Fan, J.; Wang, L. Review of Heat Conduction in Nanofluids. *J. Heat Transf.* **2011**, *133*, 097001. [[CrossRef](#)]
233. Yu, C.-J.; Richter, A.G.; Datta, A.; Durbin, M.K.; Dutta, P. Molecular Layering in a Liquid on a Solid Substrate: An X-Ray Reflectivity Study. *Phys. B Condens. Matter* **2000**, *283*, 27–31. [[CrossRef](#)]
234. Yu, W.; Choi, S.U.S. The Role of Interfacial Layers in the Enhanced Thermal Conductivity of Nanofluids: A Renovated Hamilton–Crosser Model. *J. Nanopart. Res.* **2004**, *6*, 355–361. [[CrossRef](#)]
235. Feng, Y.; Yu, B.; Xu, P.; Zou, M. The Effective Thermal Conductivity of Nanofluids Based on the Nanolayer and the Aggregation of Nanoparticles. *J. Phys. Appl. Phys.* **2007**, *40*, 3164–3171. [[CrossRef](#)]
236. Potanin, A.A.; De Rooij, R.; Van den Ende, D.; Mellema, J. Microrheological Modeling of Weakly Aggregated Dispersions. *J. Chem. Phys.* **1995**, *102*, 5845–5853. [[CrossRef](#)]
237. Shih, W.-H.; Shih, W.Y.; Kim, S.-I.; Liu, J.; Aksay, I.A. Scaling Behavior of the Elastic Properties of Colloidal Gels. *Phys. Rev. A* **1990**, *42*, 4772–4779. [[CrossRef](#)] [[PubMed](#)]
238. Chowdhury, I.; Walker, S.L.; Mylon, S.E. Aggregate Morphology of Nano-TiO₂: Role of Primary Particle Size, Solution Chemistry, and Organic Matter. *Environ. Sci. Process. Impacts* **2013**, *15*, 275–282. [[CrossRef](#)] [[PubMed](#)]
239. Prasher, R.; Phelan, P.; Bhattacharya, P. Effect of Aggregation Kinetics on the Thermal Conductivity of Nanoscale Colloidal Solutions (Nanofluid). *Nano Lett.* **2006**, *6*, 1529–1534. [[CrossRef](#)]
240. Kundan, L.; Mallick, S.S. Effect of Time Dependent Morphological Parameters of Nanoclusters on Perikinetic Heat Conduction and Induced Micro-Convection Mechanisms of Oxide Based Nanofluids. *Exp. Heat Transf.* **2018**, *31*, 251–274. [[CrossRef](#)]
241. Gao, J.W.; Zheng, R.T.; Ohtani, H.; Zhu, D.S.; Chen, G. Experimental Investigation of Heat Conduction Mechanisms in Nanofluids. Clue on Clustering. *Nano Lett.* **2009**, *9*, 4128–4132. [[CrossRef](#)]
242. Philip, J.; Shima, P.D.; Raj, B. Evidence for Enhanced Thermal Conduction through Percolating Structures in Nanofluids. *Nanotechnology* **2008**, *19*, 305706. [[CrossRef](#)]
243. Jungblut, S.; Eychmüller, A. Modeling Nanoparticle Aggregation. In *Chemical Modelling*; RSC Publishing: London, UK, 2019; pp. 1–27. [[CrossRef](#)]
244. Russel, W.B.; Saville, D.A.; Schowalter, W.R. *Colloidal Dispersions*; Cambridge University Press: Cambridge, NY, USA, 1989.
245. Sonawane, S.S.; Khedkar, R.S.; Wasewar, K.L. Effect of Sonication Time on Enhancement of Effective Thermal Conductivity of Nano TiO₂–Water, Ethylene Glycol, and Paraffin Oil Nanofluids and Models Comparisons. *J. Exp. Nanosci.* **2015**, *10*, 310–322. [[CrossRef](#)]
246. Asadi, A.; Pourfattah, F.; Miklós Szilágyi, I.; Afrand, M.; Żyła, G.; Seon Ahn, H.; Wongwises, S.; Minh Nguyen, H.; Arabkoohsar, A.; Mahian, O. Effect of Sonication Characteristics on Stability, Thermophysical Properties, and Heat Transfer of Nanofluids: A Comprehensive Review. *Ultrason. Sonochem.* **2019**, *58*, 104701. [[CrossRef](#)] [[PubMed](#)]
247. Ghadimi, A.; Metselaar, I.H. The Influence of Surfactant and Ultrasonic Processing on Improvement of Stability, Thermal Conductivity and Viscosity of Titania Nanofluid. *Exp. Therm. Fluid Sci.* **2013**, *51*, 1–9. [[CrossRef](#)]
248. Wamkam, C.T.; Opoku, M.K.; Hong, H.; Smith, P. Effects of pH on heat transfer nanofluids containing ZrO₂ and TiO₂ nanoparticles. *J. Appl. Phys.* **2011**, *109*, 024305. [[CrossRef](#)]
249. Khurana, D.; Subudhi, S. Effects of PH and Surfactant on the Forced Convection of Al₂O₃/Water and TiO₂/Water Nanofluids. *J. Therm. Sci. Eng. Appl.* **2021**, *13*, 1–18. [[CrossRef](#)]
250. Oliveira, L.R.; Silva, A.C.; Dantas, N.O.; Bandarra Filho, E.P. Thermophysical properties of TiO₂-PVA/water nanofluids. *Int. J. Heat Mass Transf.* **2017**, *1*, 795–808. [[CrossRef](#)]
251. Ouikhalfan, M.; Labihi, A.; Belaqziz, M.; Chehouani, H.; Benhamou, B.; Sari, A.; Belfkira, A. Stability and Thermal Conductivity Enhancement of Aqueous Nanofluid Based on Surfactant-Modified TiO₂. *J. Dispers. Sci. Technol.* **2020**, *41*, 374–382. [[CrossRef](#)]
252. Chakraborty, S.; Sarkar, I.; Behera, D.K.; Pal, S.K.; Chakraborty, S. Experimental Investigation on the Effect of Dispersant Addition on Thermal and Rheological Characteristics of TiO₂ Nanofluid. *Powder Technol.* **2017**, *307*, 10–24. [[CrossRef](#)]
253. Saleh, R.; Putra, N.; Wibowo, R.E.; Septiadi, W.N.; Prakoso, S.P. Titanium Dioxide Nanofluids for Heat Transfer Applications. *Exp. Therm. Fluid Sci.* **2014**, *52*, 19–29. [[CrossRef](#)]
254. Xie, H.; Fujii, M.; Zhang, X. Effect of Interfacial Nanolayer on the Effective Thermal Conductivity of Nanoparticle-Fluid Mixture. *Int. J. Heat Mass Transf.* **2005**, *48*, 2926–2932. [[CrossRef](#)]
255. Yu, W.; France, D.M.; Routbort, J.L.; Choi, S.U.S. Review and Comparison of Nanofluid Thermal Conductivity and Heat Transfer Enhancements. *Heat Transf. Eng.* **2008**, *29*, 432–460. [[CrossRef](#)]
256. Lee, S.; Choi, S.U.-S.; Li, S.; Eastman, J.A. Measuring Thermal Conductivity of Fluids Containing Oxide Nanoparticles. *J. Heat Transf.* **1999**, *121*, 280–289. [[CrossRef](#)]

257. Reynolds, O. An Experimental Investigation of the Circumstances Which Determine Whether the Motion of Water Shall Be Direct or Sinuous, and of the Law of Resistance in Parallel Channels. *Philos. Trans. R. Soc. Lond.* **1883**, *174*, 935–982.
258. Rapp, B.E. (Ed.) Chapter 9—Fluids. In *Microfluidics: Modelling, Mechanics and Mathematics*; Micro and Nano Technologies; Elsevier: Oxford, UK, 2017; pp. 243–263. [[CrossRef](#)]
259. Fedele, L.; Colla, L.; Bobbo, S. Viscosity and Thermal Conductivity Measurements of Water-Based Nanofluids Containing Titanium Oxide Nanoparticles. *Int. J. Refrig.* **2012**, *35*, 1359–1366. [[CrossRef](#)]
260. Hojjat, M.; Etemad, S.; Bagheri, R.; Thibault, J. Thermal Conductivity of Non-Newtonian Nanofluids: Experimental Data and Modeling Using Neural Network. *Int. J. Heat Mass Transf.* **2011**, *54*, 1017–1023. [[CrossRef](#)]
261. Batmunkh, M.; Tanshen, R.; Nine, J.; Myekhlai, M.; Choi, H.; Chung, H.; Jeong, H. Thermal Conductivity of TiO₂ Nanoparticles Based Aqueous Nanofluids with an Addition of a Modified Silver Particle. *Ind. Eng. Chem. Res.* **2014**, *53*, 8445–8451. [[CrossRef](#)]
262. Duangthongsuk, W.; Wongwises, S. Measurement of Temperature-Dependent Thermal Conductivity and Viscosity of TiO₂-Water Nanofluids. *Exp. Therm. Fluid Sci.* **2009**, *33*, 706–714. [[CrossRef](#)]
263. Shrestha, S.; Wang, B.; Dutta, P. Nanoparticle Processing: Understanding and Controlling Aggregation. *Adv. Colloid Interface Sci.* **2020**, *279*, 102162. [[CrossRef](#)]
264. Kamiya, H.; Gotoh, K.; Shimada, M.; Uchikoshi, T.; Otani, Y.; Fujii, M.; Matsusaka, S.; Matsuyama, T.; Tatami, J.; Higashitani, K.; et al. Characteristics and behavior of nanoparticles and its dispersion system. In *Nanoparticle Technology Handbook*; Hosokawa, M., Nogi, K., Naito, M., Yokoyama, T., Eds.; Elsevier: Amsterdam, The Netherlands, 2008; pp. 113–176. [[CrossRef](#)]
265. Fan, W.; Zhong, F. Effects of Macroparameters on the Thickness of an Interfacial Nanolayer of Al₂O₃- and- and TiO₂-Water-Based Nanofluids. *ACS Omega* **2020**, *5*, 27972–27977. [[CrossRef](#)]
266. Li, Z.H.; Gong, Y.J.; Pu, M.; Wu, D.; Sun, Y.H.; Wang, J.; Liu, Y.; Dong, B.Z. Determination of Interface Layer Thickness of a Pseudo Two-Phase System by Extension of the Debye Equation. *J. Phys. Appl. Phys.* **2001**, *34*, 2085–2088. [[CrossRef](#)]
267. Berger, F.; Dékány, I. Variable Thickness of the Liquid Sorption Layers on Solid Surfaces. *Colloids Surf. A Physicochem. Eng. Asp.* **1998**, *141*, 305–317. [[CrossRef](#)]
268. Chandrasekar, M.; Suresh, S.; Srinivasan, R.; Bose, A.C. New Analytical Models to Investigate Thermal Conductivity of Nanofluids. *J. Nanosci. Nanotechnol.* **2009**, *9*, 533–538. [[CrossRef](#)]
269. Murshed, S.M.S.; Leong, K.C.; Yang, C. Enhanced Thermal Conductivity of TiO₂—Water Based Nanofluids. *Int. J. Therm. Sci.* **2005**, *44*, 367–373. [[CrossRef](#)]
270. Wei, W.; Cai, J.; Hu, X.; Han, Q.; Liu, S.; Zhou, Y. Fractal Analysis of the Effect of Particle Aggregation Distribution on Thermal Conductivity of Nanofluids. *Phys. Lett. A* **2016**, *380*, 2953–2956. [[CrossRef](#)]
271. Gao, T.; Jelle, B.P. Thermal Conductivity of TiO₂ Nanotubes. *J. Phys. Chem. C* **2013**, *117*, 1401–1408. [[CrossRef](#)]
272. Ali, S.; Orell, O.; Kanerva, M.; Hannula, S.-P. Effect of Morphology and Crystal Structure on the Thermal Conductivity of Titania Nanotubes. *Nanoscale Res. Lett.* **2018**, *13*, 212. [[CrossRef](#)]
273. Yang, L.; Wang, C.-Z.; Lin, S.; Chen, T.; Cao, Y.; Zhang, P.; Liu, X. Thermal Conductivity of TiO₂ Nanotube: A Molecular Dynamics Study. *J. Phys. Condens. Matter* **2018**, *31*, 055302. [[CrossRef](#)]
274. Ali, N.; Bahman, A.M.; Aljuwayhel, N.F.; Ebrahim, S.A.; Mukherjee, S.; Alsayegh, A. Carbon-Based Nanofluids and Their Advances towards Heat Transfer Applications—A Review. *Nanomaterials* **2021**, *11*, 1628. [[CrossRef](#)]
275. Behabtu, N.; Young, C.C.; Tsentelovich, D.E.; Kleinerman, O.; Wang, X.; Ma, A.W.K.; Bengio, E.A.; ter Waarbeek, R.F.; de Jong, J.J.; Hoogerwerf, R.E.; et al. Strong, Light, Multifunctional Fibers of Carbon Nanotubes with Ultrahigh Conductivity. *Science* **2013**, *339*, 182–186. [[CrossRef](#)]
276. Chen, H.; Witharana, S.; Jin, Y.; Kim, C.; Ding, Y. Predicting Thermal Conductivity of Liquid Suspensions of Nanoparticles (Nanofluids) Based on Rheology. *Particuology* **2009**, *7*, 151–157. [[CrossRef](#)]
277. Chen, H.; Yang, W.; He, Y.; Ding, Y.; Zhang, L.; Tan, C.; Lapkin, A.A.; Bavykin, D.V. Heat Transfer and Flow Behaviour of Aqueous Suspensions of Titanate Nanotubes (Nanofluids). *Powder Technol.* **2008**, *183*, 63–72. [[CrossRef](#)]
278. Kasuga, T.; Hiramatsu, M.; Hoson, A.; Sekino, T.; Niihara, K. Titania nanotubes prepared by chemical processing. *Adv. Mater.* **1999**, *11*, 1307–1311. [[CrossRef](#)]